Hydroxo-bridged active site of a flavodiiron NO reductase revealed by spectroscopy and computations

Filipe Folgosa,[a,§] Vladimir Pelmenschikov,[b,*,§] Matthias Keck,[c] Christian Lorent,[b] Yoshitaka Yoda,[d] James A. Birrell,[e] Martin Kaupp,[b] Miguel Teixeira,[a] Kenji Tamasaku,[f] Christian Limberg,[c] Lars Lauterbach[b,*]

[a] *Instituto de Tecnologia Química e Biológica António Xavier, ITQB NOVA, Av. da República, 2780-157 Oeiras, Portugal*

[b] *Institut für Chemie, Technische Universität Berlin, 10623 Berlin, Germany. E-mail: lars.lauterbach@tu-berlin.de ; pelmentschikov@tu-berlin.de*

[c] *Department of Chemistry, Humboldt-Universität zu Berlin, Brook-Taylor-Strasse 2, 12489 Berlin, Germany*

[d] *JASRI, SPring-8, Sayo-gun, Hyogo 679-5198, Japan*

[e] *Max Planck Institute for Chemical Energy Conversion, Stiftstrasse 34-36, 45470 Mülheim an der Ruhr, Germany*

[f] *RIKEN SPring-8 Center, Sayo-gun, Hyogo 679-5148, Japan*

* Corresponding authors. § These authors contributed equally.

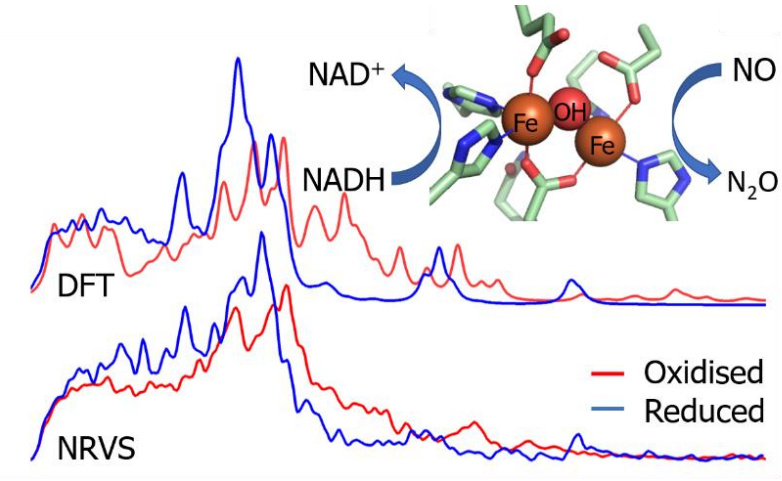

Abstract: NO and O_2 are detoxified in many organisms using flavodiiron proteins (FDPs). The exact coordination of the iron centre in the active site of these enzymes remains unclear in spite of numerous structural studies. Here, we used ^{57}Fe nuclear resonance vibrational spectroscopy (NRVS) to probe the iron-ligand interactions in *Escherichia coli* FDP. This data combined with density functional theory (DFT) and ^{57}Fe Mössbauer spectroscopy indicate that the oxidised form of FDP contains a dihydroxo-diferric Fe(III)–$(\mu OH^-)_2$–Fe(III) active site, while its reduction gives rise to a monohydroxo-diferrous Fe(II)–(μOH^-)–Fe(II) site upon elimination of one bridging OH^- ligand, thereby providing an open coordination site for NO binding. Prolonged NRVS data collection of the oxidised FDP sample resulted in photoreduction and formation of a partially reduced diiron centre with two bridging hydroxo ligands. These results have crucial implications for studying and understanding the mechanism of FDP as well as other non-haem diiron enzymes.

Introduction

Nitric oxide (NO) inhibits multiple cellular processes including aerobic respiration and energy metabolism.[1] Therefore, NO is produced in response to pathogens by the human innate immune system. In order to survive this threat, microbes utilise several enzymes to detoxify NO. Among these are the flavodiiron proteins (FDPs), which reduce it to the innocuous N_2O.[2, 3] FDPs have a minimal core constituted by a metallo-β-lactamase-like domain, containing the catalytic diiron centre, and a flavodoxin-like domain with a flavin mononucleotide (FMN). The FDP from *Escherichia coli* (*Ec*FDP) has an extra rubredoxin-like domain at its C-terminus, which is important for electron transfer as the electron entry point.[3, 4] Although some FDPs are able to reduce O_2 to H_2O or NO to N_2O, most of them cannot accomplish these reactions at the same rate, showing preference to one of the substrates.[5] The *Ec*FDP is the only known FDP with a clear preference for NO over O_2, exhibiting a rate of ca. 10 times higher for the NO reduction. Electrons for this reaction are transferred from NADH *via* an NADH:flavorubredoxin oxidoreductase.[5, 7]

Several three-dimensional structures of FDPs have been determined by X-ray crystallography, which disclosed that the diiron active site is coordinated by four histidines, two aspartates, one glutamate and one μ-hydroxo bridge (Figs. 1 and S8).[6, 8, 9] With two histidines at each Fe and one bridging bidentate carboxylate of Asp166, the FDP metal-ligand core bears an approximate reflection symmetry. Similar non-haem diiron centres are found in a variety of other proteins, such as soluble methane monooxygenase, Δ9-desaturase, ribonucleotide reductase, (bacterio)ferritin, toluene monooxygenase, haemerythrin, and rubrerythrin.[10]

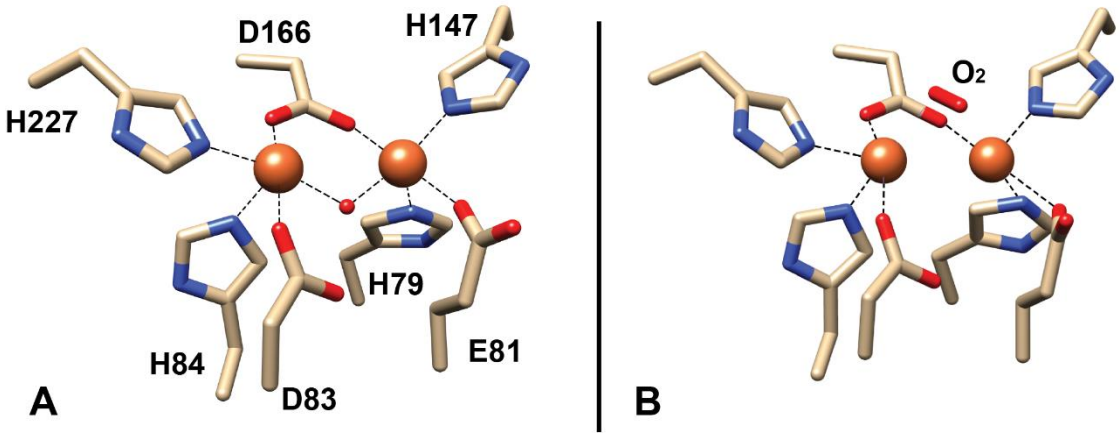

Fig. 1 Representation of the active site of the *E. coli* flavodiiron protein obtained by X-ray crystallography. **A**: structure in the as-isolated (oxidised) form (PDB 4D02). **B**: structure of the dithionite-reduced crystal (PDB 5LLD). Orange spheres represent iron. The structure represented in **A** shows a μ-hydroxo (μOH^-) ligand bridging the two iron ions, while the structure represented in **B** shows a dioxygen molecule in the vicinity of the diiron centre.[6] The phosphate ion present in the as-isolated protein structure was omitted for clarity.

The structural studies also showed that, in general, non-haem diiron active sites can harbour at least one mononuclear oxygen metal ligand in the Fe(III)Fe(III) oxidised state. Many structures of the Fe(II)Fe(II) reduced states reveal a bridging mononuclear oxygen species, which is missing in the *Ec*FDP structure (Table S1).[6, 8, 11-13] However, the discrimination between oxo and hydroxo bridging ligands has been precluded by insufficient resolution of the crystal structures available. Spectroscopic studies on an O_2-selective FDP from *Thermotoga maritima* (*Tm*FDP) suggest that NO reduction to N_2O follows a sequential binding of two NO molecules to the reduced diiron centre, forming mono- and dinitrosyl intermediates.[14] The detection of an intermediate species, assigned to an antiferromagnetically coupled diferrous-dinitrosyl species with an exchange energy J = 60 cm^{-1} point to a hydroxo bridge between the two Fe(II)–NO centres that could be important for the N−N bond formation.[14] It was also proposed that, contrary to what was found in the *Tm*FDP (PDB 1VME) and *Ec*FDP (PDB 4D02)[6] crystal structures, the *Tm*FDP harbours two bridging hydroxo ligands coordinated in the oxidised state, one of which is lost in the diferrous state.[15] This implies that the mono-μ-hydroxo diferrous FDP species is probably the catalytically functional state that reacts with the substrates.

The enzymatic NO conversion mechanism of *Ec*FDP, which is the only known NO-specific FDP, is key to understanding one of the most important microbial NO detoxification pathways. Here, we investigate the diiron coordination of *Ec*FDP in its oxidised and reduced states using ^{57}Fe nuclear resonance vibrational (NRVS) and Mössbauer, spectroscopies combined with density functional theory (DFT) calculations.

Results and Discussion

A truncated derivative of *Ec*FDP (residues 1-400) was used as our model system, hereafter referred to as FDP-D, in order to avoid the ^{57}Fe signal interference from the rubredoxin domain, otherwise naturally present in the native protein. FDP-D showed comparable spectroscopic and biochemical properties to native *Ec*FDP.[7] FDP-D was enriched with ^{57}Fe and prepared as described in the ESI.

Zero-field Mössbauer spectra of the as-isolated (oxidised, FDP-D_{OX}) and dithionite reduced (FDP-D_{RED}) protein samples at 13 K are shown in Fig. 2. The spectrum of FDP-D_{OX} is similar to that of *Tm*FDP.[15, 16] The fits of the zero-field spectra deconvoluted the signals of two unequal Fe ions with the parameters listed in Table 1 (Fig. S1). The isomer shifts (δ = 0.50 and 0.49 mm/s) and quadrupole splitting parameters (ΔE_Q = 0.70 and 1.00 mm/s) indicate that both iron species are high-spin Fe^{3+}. A previous study with *Tm*FDP showed that at 4.2 K, the two high-spin (S = 5/2) Fe^{3+} ions are exchange-coupled antiferromagnetically to produce a diamagnetic (S = 0) ground state.[15] In agreement with this observation, FDP-D_{OX} is EPR-silent.[7]

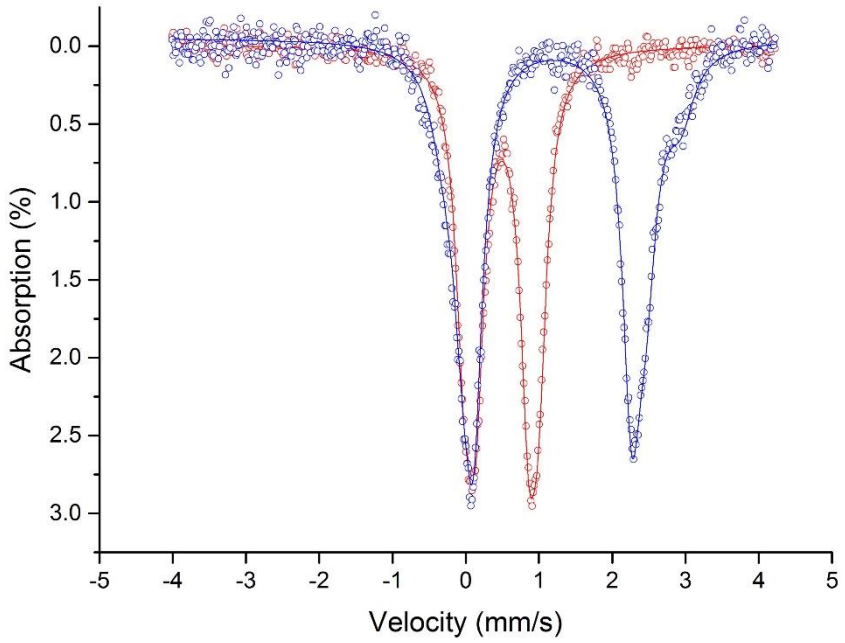

Fig. 2 Zero-field Mössbauer spectra (dots) and fittings (lines) of as-isolated FDP-D_{OX} (red) and reduced FDP-D_{RED} (blue) samples, recorded at 13 K. Mössbauer parameters are presented in Table 1.

The Mössbauer parameters were also compared to other non-haem diiron enzymes (Table S1). The most similar to FDP-D_{OX} were those of soluble methane monooxygenase (sMMO), which contains two hexacoordinated iron ions connected by two bridging hydroxo ligands in its oxidised state.[17,12]

Reduction with dithionite leads to a significant change in the spectrum (Figs. 2 and S3). The zero-field Mössbauer spectrum of FDP-D_{RED} showed quadrupole doublets with parameters indicative of high-spin (S = 2) Fe^{2+} (Table 1) as observed for reduced *Tm*FDP.[15] Besides the contribution of the two main species consistent with pentacoordinated iron centres, the spectrum also presents a third minor feature (13 %) that shows a higher ΔE_Q value, possibly due to a hexacoordinated centre indicating a modified amino acid coordination or free iron in solution.[18] The spectra at 120 K and at 13 K in the presence of an external magnetic field of 37 mT, applied parallel to the γ-ray direction, were nearly identical to the zero-field Mössbauer spectrum of FDP-D_{RED} at 13 K (Fig. S2). A comparison of the Mössbauer parameters of iron species #1 and #2 with other non-haem diiron enzymes (Table S1) suggests a pentacoordinated structure with one μ-hydroxo ligand such as in reduced ribonucleotide reductase or sMMO.[12, 13, 17, 19]

Table 1: Mössbauer parameters of as-isolated and reduced FDP-D. Symbols: δ = isomer shift, ΔE_Q = quadrupole splitting, Γ = line width at half maximum, I = intensity contribution.

Sample	Species Number	δ (mm/s)	ΔE_Q (mm/s)	Γ (mm/s)	I (%)
FDP-D_{OX}	#1	0.50	0.71	0.28	50
	#2	0.49	1.00	0.29	50
FDP-D_{RED}	#1	1.18	2.14	0.29	43.5
	#2	1.20	2.46	0.38	43.5
	#3	1.32	3.23	0.44	13

In order to unequivocally determine the structure of the FDP active site, vibrational spectroscopy was employed. Initial resonance Raman (RR) spectroscopic experiments on FDP-D lacked resonance enhanced metal ligand vibrations[20] and gave only signals arising from intrinsic FMN (Fig. S6). In contrast to the traditional infrared (IR) and RR techniques prone to their selection rules, a distinct advantage of NRVS is that it detects all vibrational modes with ^{57}Fe nuclei motion, thus having high specificity and sensitivity to the iron centres.[21, 22]

Our first NRVS data of FDP-D_{OX} showed changes to the spectra during the 20 h of data collection (Fig. S7). Mössbauer spectra recorded after the 20 h NRVS measurements (Fig. S5) revealed two new additional iron species with a total of 12% contribution (Table S2). The fitted isomer shifts (δ = 1.28 and 1.24 mm/s) and quadrupole splittings (ΔE_Q = 2.03 and 2.70 mm/s) correspond to high-spin Fe^{2+}, which indicates partial photoreduction of the active site by the 14.4 keV X-rays. Here, the two Fe^{2+} Mössbauer species are tentatively associated with either iron site photoreduced.

Three other oxidised FDP-D samples from the same preparation were investigated by NRVS for 4, 6, and 10 h data collection times, respectively, and their Mössbauer spectra were subsequently recorded (Fig. S4). No changes were identified after 4 h, while after 6 h the Mössbauer spectrum changed slightly and after 10 h a total intensity of approximately 8% of two high-spin Fe^{2+} species was detected (Table S2). Thus, only the first NVRS spectra measured up to 4 h were considered for calculating the ^{57}Fe partial vibrational density of states (PVDOS) of FDP-D_{OX} (Fig. 3).

The NRVS of FDP-D_{OX} displays three major bands in the 200-300 cm^{-1} vibrational energy region, broader features in the 300-400 cm^{-1} region, and smaller intensity peaks at 471 cm^{-1} and 527 cm^{-1} with additional shoulders. Previous NRVS and DFT studies of a series of high-spin

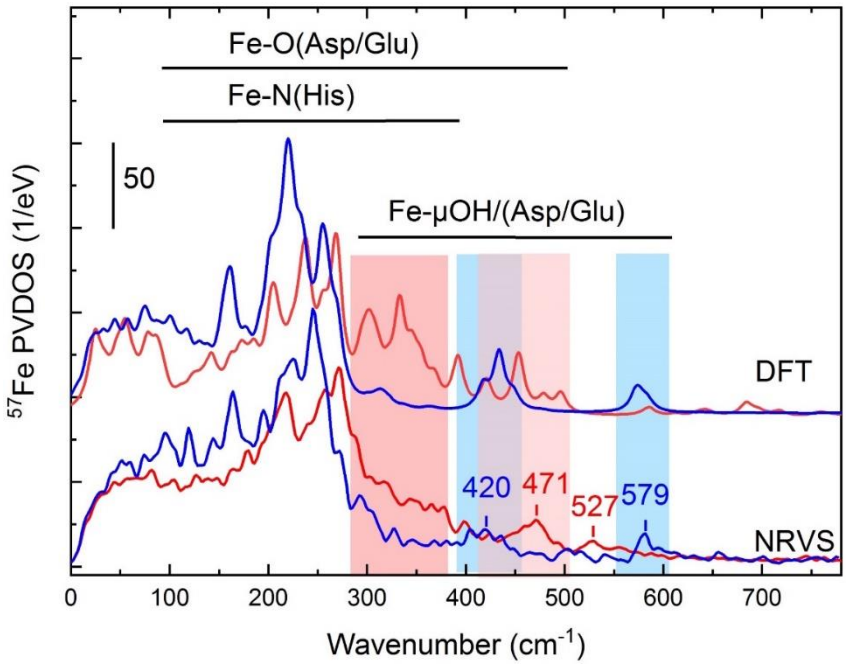

Fig. 3 ^{57}Fe-PVDOS spectra of FDP-D in the as-isolated FDP-D_{OX} (red) and reduced FDP-D_{RED} (blue) states from NRVS experiments (bottom) and DFT calculations (top). The vibrational signatures for the diiron active site with histidine, glutamate, aspartate and bridging μOH^- ligands are shown. Redox-dependent changes are indicated by red and blue bars. An alternative comparison of these spectra is available in Fig. S18.

Fe(III)Fe(III) model compounds showed that mainly Fe/O/N core vibrational modes contributed to the bands between 200 and 300 cm^{-1}.[23] The corresponding Fe-O stretches of mono-oxo, peroxo and di-oxo/hydroxo bridging ligands were identified between 350 and 600 cm^{-1}. Remarkably, our NRVS data of FDP-D_{OX} correspond better with the di-oxo/hydroxo than with the mono-oxo compounds.[23]

The reduction of FDP-D resulted in a red shift of the bands below 350 cm^{-1} (Fig. 3). The Mössbauer spectra for the pre-NRVS and post-NRVS FDP-D_{RED} samples were nearly identical (not shown), which indicates that no radiation damage occurred. The red shift is consistent with the Fe(III)Fe(III) to Fe(II)Fe(II) reduction, resulting in longer metal-ligand bond lengths.[21] The reduced FDP-D shows more intense features mostly in the lower-energy region at 163 cm^{-1} and between 185 cm^{-1} and 275 cm^{-1}. At higher energies, a feature with two shoulders appears at 420 cm^{-1} and a distinct peak at 579 cm^{-1}. The two high-energy features are analogous to Fe(III)-μO-Fe(III) compounds showing symmetric Fe-O stretches in the ~530-550 cm^{-1} region, and anti-symmetric Fe-O stretches in the ~710-750 cm^{-1} region.[23-26] A recent NRVS study of a series of trigonal bipyramidal Fe(III)-hydroxo and -oxo complexes with varying H-bonding networks showed that even subtle changes in the H-network resulted in significant shifts of the Fe–O(H) vibrational frequencies.[27]

Protonation of an oxo ligand caused a large ~180 cm^{-1} red shift in the energy of the stretching Fe-O band to ~480 cm^{-1} and elongation of the Fe-O(H) bond. The lower energy bands of FDP-D_{RED} can therefore be explained by the reduction of the diiron centre resulting in longer bonds, a bridging hydroxo instead of an oxo species, or a change in the hydrogen bond network.

A broad set of in total 28 alternative DFT models of the FDP active site has been computationally explored, invariantly containing seven side chains binding the two Fe ions as described in the ESI methods section, targeting the reproduction of the NRVS-observed FDP-$D_{OX/RED}$ spectra. The structural alternatives involved modifications of the bridging oxygenous ligands, their number, and protonation level. These included primarily hydroxo OH^- species as well as water H_2O, peroxo O_2^{2-}, superoxo $O_2^{\bullet-}$, and oxo O^{2-} Fe ligands, or a vacant bridging site. Following X-ray structural data (Fig. S8),[6, 8] O_2 and H_2O molecules weakly bound in the FDP active site pocket have been further considered, as well as a bidentate phosphate anion PO_4^{3-} coordination observed in the crystal structure of the oxidised state of *Ec*FDP (Fig. S8). The calculations generally relied on broken-symmetry[28] (BS) solutions implying antiferromagnetic coupling between the two high-spin homovalent iron sites and approximating the diamagnetic (total $S = 0$) state. Furthermore, alternative electronic states as well as mixed-valence (total $S = 1/2$) Fe(III)Fe(II) diiron cores were explored. All these models are described in the Supplementary Results section of ESI, with their structures and ^{57}Fe-PVDOS spectra displayed correspondingly in Figs. S9-S17 and Figs. S18-S26.

Considered as candidates representing a pure sample, many DFT models are in apparent conflict with the collected NRVS data. The best fit between the NRVS-observed and DFT-calculated ^{57}Fe-PVDOS signatures (Figs. 3 and S18) for the FDP-D_{RED} and FDP-D_{OX} states were produced by configurations described as Fe(III)–(μOH^-)$_2$–Fe(III) and Fe(II)–(μOH^-)–Fe(II), respectively. Both the oxidised and reduced state models (Fig. 4 and Figs. S9, S10) retain pseudo reflection symmetries of their metal-ligand cores, where the mirror plane passes between the two Fe sites and encompasses the μOH^- ligand(s).

DFT optimisations further suggest approximate arrangements of the FDP active site, where the four iron-imidazole Fe(III)–N(His) coordinations are coplanar with the oxidised iron-hydroxo Fe(III)–(μOH^-)$_2$–Fe(III) core, and four iron-carboxylate Fe(II)–O(Asp,Glu) coordinations are coplanar with the reduced Fe(II)–(μOH^-)–Fe(II) core (Fig. 4). While the FDP-D_{OX} state shows two hexacoordinate Fe(III) sites, reductive elimination of one μOH^- ligand produces the FDP-D_{RED} state with two pentacoordinate Fe(II) sites and the remaining μOH^- position in qualitative agreement with the X-ray structural reference (Fig. S8).[6, 8] This redox-dependent active site transformation largely follows a recent rationalisation by Weitz *et al.* for an O_2-selective FDP,[15] and agrees with our Mössbauer results outlined above.

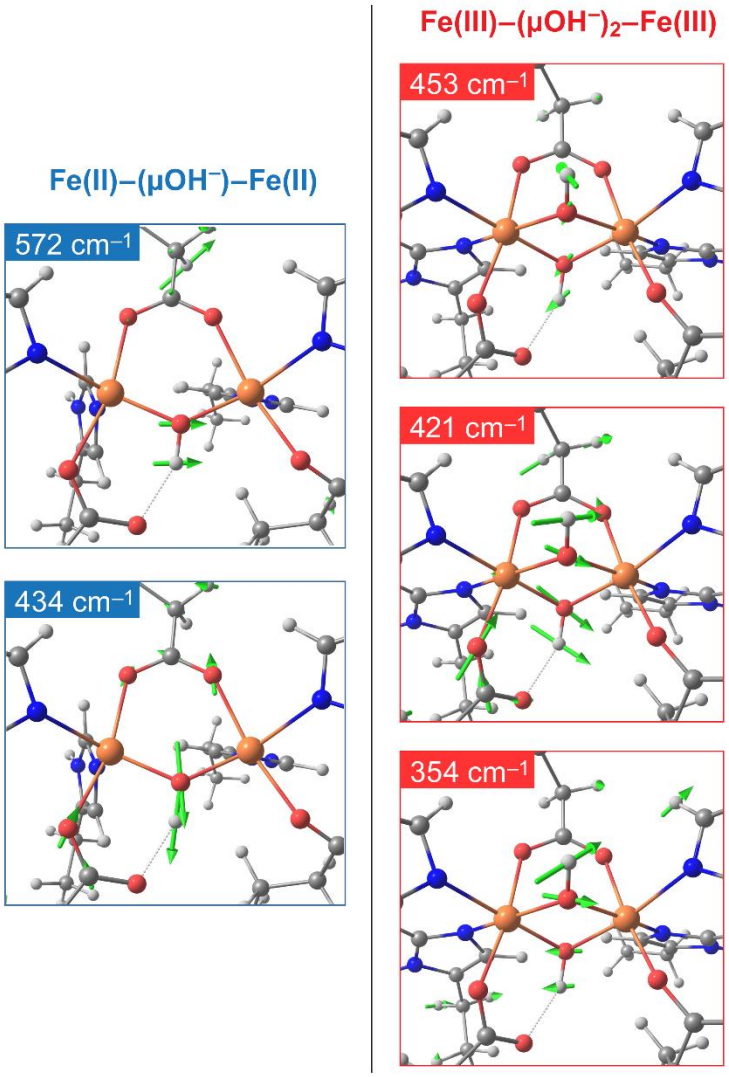

Fig. 4 Important Fe–μOH⁻ normal modes shown as green arrows for the reduced (left) and oxidised (right) DFT models of the FDP-D active site, with their vibrational energies (cm^{-1}) provided. The individual mode intensities in context of the ^{57}Fe-PVDOS (NRVS) spectra are indicated in Fig. S18. These and other normal mode animations are available as part of the ESI.

An important redox-invariant determinant, presently deduced for both the FDP-$D_{RED/OX}$ structures, is the hydrogen bonding between the bridging hydroxo ligand and the Asp83 carboxylate oxygen (Figs. 4 and 5). The characteristic μO(H)···O(Asp) interaction at ~2.5-2.8 Å, as commonly found for a homologous aspartate in the FDP crystal structures, compares well with the DFT-optimized distance of ~2.7-2.8 Å. A local minimum avoiding the μOH···O(Asp83) hydrogen bond was found more unfavourable by 10 kcal/mol and produced an inferior match to the FDP-D_{RED} NRVS data (Figs. S12 and S21a).

Figs. 3 and S18 display a significant overlap between the NRVS-observed and DFT-calculated ^{57}Fe-PVDOS signatures, including their redox-dependent changes. Recalling the NRVS analysis from the previous section, both experiment and theory indicate a consistent redistribution of the Fe nuclear motion during the redox event: while the FDP-D_{OX} state spectral

intensity gradually declines up to ~500-600 cm^{-1}, the FDP-D_{RED} state instead displays a well-defined cutoff of the high-intensity region at ~300 cm^{-1}. This redox-dependent spectral difference results from the compressed and dihydroxo-bridged Fe(III)–$(\mu OH^{-})_2$–Fe(III) core with a shortened Fe···Fe = 3.06 Å optimised distance. The monohydroxo-bridged Fe(II)–(μOH^{-})–Fe(II) core with a longer Fe···Fe = 3.53 Å distance instead produces normal modes with a lesser degree of vibrational coupling between the two Fe sites. Among the two types of FDP protein ligands, the four carboxylates are the ones that move ~0.1-0.2 Å further away from the metal sites upon reduction, thereby redistributing the Fe–O(Asp,Glu) vibrations within their ~100-500 cm^{-1} range to predominantly lower frequencies. The metal-to-imidazole distances, however, remain essentially redox unaffected, together with the corresponding Fe–N(His) vibrational pattern within ~100-400 cm^{-1}. The oxidised FDP-D_{OX} state DFT model, in contrast to FDP-D_{RED}, showed a significantly higher number of mixed Fe–μOH^{-}/O(Asp,Glu) vibrations in the ~300-400 cm^{-1} region, all contributing to the ^{57}Fe-PVDOS. Another difference here is the prediction of mixed Fe–μO–H bending modes in the ~600-800 cm^{-1} region exclusively in FDP-D_{OX} (vs. >800 cm^{-1} in FDP-D_{RED}) with their small ^{57}Fe-PVDOS intensities at the level of the experimental error. The effects listed above can be traced in the ^{57}Fe–μOH^{-}/O(Asp,Glu)/N(His) KED profiles shown in Fig. S19 as well as in the DFT-based normal mode animations provided as part of the ESI.

In the high-intensity region below 300 cm^{-1}, two prominent and matching bands in the FDP-D_{RED} NRVS/DFT spectra are correspondingly at 245/220 (global maximum) and 164/161 cm^{-1} (Fig. S18a). In contrast, NRVS/DFT ^{57}Fe-PVDOS of FDP-D_{OX} shows a blue-shifted and diminished-intensity global maximum at correspondingly 271/268 cm^{-1}, with a 2nd-highest intensity band at 218/237 cm^{-1} (Fig. S18b). Regardless of the oxidation states, the aforementioned bands represent Fe–His/Asp/Glu stretches and bends, where the entire imidazole and carboxylate groups participate in vibration.

In the region above 300 cm^{-1}, the matching NRVS/DFT ^{57}Fe-PVDOS features of FDP-D_{RED} are correspondingly at (*i*) ~400-440/420-450 cm^{-1} (with maxima at 419/434 cm^{-1}) and (*ii*) at 581/574 cm^{-1}. Employing the FDP active site approximately mirror plane symmetry, DFT rationalises these bands as correspondingly (*i*) in-plane and (*ii*) out-of-plane iron-hydroxo Fe–μOH^{-} vibrations (Fig. 4, left). The two ^{57}Fe-PVDOS features are produced by several normal modes each, due to the vibrational coupling between μOH^{-} and carboxylates from the terminal Asp83 and bridging Asp166 Fe ligands. These couplings have correspondingly (*i*) Fe–O(Asp) stretching and (*ii*) Fe–O–C(Asp) bending character. In comparison, FDP-D_{OX} shows a tentatively matching NRVS/DFT band at 471/453 cm^{-1}, with the underlying DFT normal mode of mostly in-

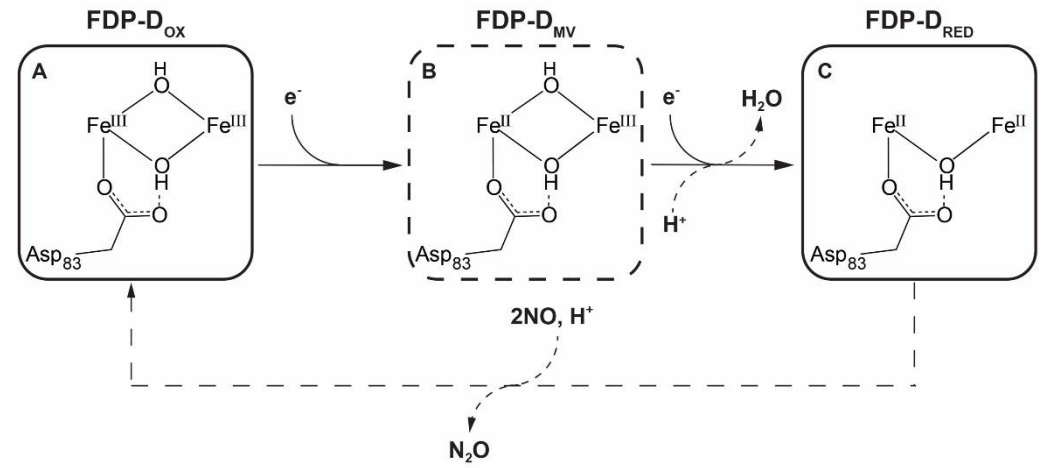

Fig. 5 Diiron core structures of *Ec*FDP in the fully oxidized FDP-D_{OX} (**A**), mixed-valence FDP-D_{MV} (**B**) and reduced FDP-D_{RED} (**C**) states, proposed in this study. The amino acids other than Asp83 were omitted for clarity. Representation of the FDP-D_{OX} and FDP-D_{RED} species arise from the NRVS experiment and DFT calculations. The proposal of the FDP-D_{MV} species is based on the DFT calculation performed to adjust to the contribution of a mixed-valence state detected upon photoreduction promoted by prolonged NRVS data collection. The dashed line in the lower part of the scheme represents the reaction with the substrate, NO, during the catalytic cycle.

plane character (*i* above), where the two μOH$^-$ ligands displace in-phase (Fig. 4, right panel). From the DFT calculations, the out-of-plane (μOH$^-$)$_2$ modes (*ii* above) of FDP-D_{OX} appear at lower energies, 421 cm^{-1} (symmetric) and 354 cm^{-1} (asymmetric), where they become mixed with the Fe–O(Asp,Glu)/N(His) vibrations having higher ^{57}Fe-PVDOS intensities compared to the isolated Fe–μOH$^-$ motions. The vibrational energy order of modes type (*i*) and (*ii*) is therefore opposite in FDP-D_{OX} and FDP-D_{RED}, but in both states the type (*i*) in-plane μOH$^-$ normal modes produce higher individual ^{57}Fe-PVDOS intensities (Fig. S18).

For the photoreduced species upon prolonged NRVS data collection (see above), alternative DFT models of the FDP active site were examined. Indeed, the presence of a 24% contribution of a mixed-valence Fe(III)–(μOH)$_2$–Fe(II) state (FDP-D_{MV}) is in a good agreement with the changes of the experimental NRVS data based on the 17-20 h collection interval (Figs. S7 and S20b), as well as the post-NRVS Mössbauer data (Fig. S5). Although red-shifted global spectral maxima at vibrational energies below 220 cm^{-1} might be explained by a contribution of a diferrous Fe(II)–(μOH$^-$)$_2$–Fe(II) species (Fig. S20a), the better performance of the (partially) reduced models with two rather than one bridging hydroxo ligands (Fig. S20) indicate an active site structure similar to that of the oxidised state (Fig. S11 bottom). This is logical, considering how unlikely it is for ligand dissociation to occur under cryogenic conditions. A mixed-valence species, that has also been observed by EPR spectroscopy upon reduction with 1 equivalent of menadiol,[7] might represent an intermediate during catalysis (Fig. 5).

Conclusions

In conclusion, the first combined NRVS, DFT and Mössbauer characterisation of a non-haem diiron enzyme has addressed the active site composition and redox-dependent changes

in the NO-converting *Ec*FDP. We demonstrated the presence of two bridging hydroxo ligands in the oxidised state, and one bridging hydroxo ligand in the reduced state (Fig. 5). This finding unravels a discrepancy between the Fe-ligand configurations found in the crystal structures of *Ec*FDP as compared with the now determined solution structures of this enzyme. We identified photoreduction of the as-isolated (oxidised) sample upon prolonged NRVS data collection. Our data suggest the formation of a partially reduced species (the mixed-valence state) with two bridging hydroxo ligands (Fig. 5). Future studies in terms of NRVS-monitored X-ray photoreduction may provide additional spectroscopic insights on non-haem diiron metalloenzymes. Furthermore, our approach provided access to the redox-dependent vibrational signature of the FDP active site. Vibrational bands arising from the μOH^{-} motions, predominantly either parallel or perpendicular to the Fe···Fe vector, were identified. Alternative diiron cores with ligands either different to hydroxo, or with the vacant bridging site, are clearly disfavoured as significant components in our *Ec*FDP-D samples. ^{57}Fe-NRVS spectroscopy, applied here in conjunction with DFT modelling, proves itself as a useful method for addressing metalloenzyme´s iron coordination in its fine detail and demonstrated the pioneering resolution of protein Fe–OH vibrational bands. We conclude that a di-μ-hydroxo diferric species (in the as-isolated enzyme) is reduced to a mono-μ-hydroxo diferrous state, the functional form ready to react with the NO substrate. An extension of this approach to catalytic intermediates in flavodiiron enzymes will provide valuable information about their structure, thereby opening novel perspectives in gas-converting chemistry.

Author Contributions

L.L. and M.T. conceived and designed the research; F.F. prepared the protein samples; M.K.[c] acquired the Mössbauer spectra; C.L.[b] acquired the resonance Raman spectra; L.L. and J.A.B. collected the NRVS data with assistance by Y.Y. and K.T.; V.P. performed the DFT calculations; F.F., V.P., M.K.[c], C.L.[b], J.A.B., M.K.[b], M.T., C.L.[c], and L.L. contributed to the data analysis and participated in the discussions. F.F., V.P., and L.L. wrote the manuscript with input from all authors. (Contributions from [b]Technische Universität Berlin and [c]Humboldt-Universität zu Berlin.)

Conflicts of interest

There are no conflicts to declare.

Acknowledgements

This work was funded through Fundação para a Ciência e a Tecnologia, Portugal, Project PTDC_BIA-BQM_27959_2017 (to M.T.) and by MOSTMICRO-ITQB with refs UIDB/04612/2020 and UIDP/04612/2020. This project has also received funding from the European Union's

Horizon 2020 research and innovation programme under grant agreement Nº 810856. L.L, C.L., M.K. and V.P. received funding by the Deutsche Forschungsgemeinschaft (DFG, German Research Foundation) under Germany´s Excellence Strategy – EXC 2008 – 390540038 – UniSysCat. J.A.B. acknowledges the Max Planck Society and DFG Priority Programme "Iron-Sulfur for Life: Cooperative Function of Iron-Sulfur Centers in Assembly, Biosynthesis, Catalysis and Disease" (SPP 1927) Project BI 2198/1-1 for funding. We thank Oliver Lenz for generous support by using his lab equipment and Peter Hildebrandt, Stephen P. Cramer, Hongxin Wang and Leland B. Gee for helpful discussions. NRVS experiments at BL19LXU of SPring8 were approved under proposal no. 2020A1450, 2016B1316.

Notes and references

1. A. M. Gardner, R. A. Helmick and P. R. Gardner, *J. Biol. Chem.*, 2002, **277**, 8172-8177.
2. R. Silaghi-Dumitrescu, E. D. Coulter, A. Das, L. G. Ljungdahl, G. N. Jameson, B. H. Huynh and D. M. Kurtz, Jr., *Biochemistry*, 2003, **42**, 2806-2815.
3. C. M. Gomes, A. Giuffre, E. Forte, J. B. Vicente, L. M. Saraiva, M. Brunori and M. Teixeira, *J. Biol. Chem.*, 2002, **277**, 25273-25276.
4. F. Folgosa, M. C. Martins and M. Teixeira, *FEMS Microbiol. Lett.*, 2018, **365**.
5. M. C. Martins, C. V. Romão, F. Folgosa, P. T. Borges, C. Frazão and M. Teixeira, *Free Radical Biol. Med.*, 2019, **140**, 36-60.
6. C. V. Romao, J. B. Vicente, P. T. Borges, B. L. Victor, P. Lamosa, E. Silva, L. Pereira, T. M. Bandeiras, C. M. Soares, M. A. Carrondo, D. Turner, M. Teixeira and C. Frazao, *J. Mol. Biol.*, 2016, **428**, 4686-4707.
7. J. B. Vicente and M. Teixeira, *J. Biol. Chem.*, 2005, **280**, 34599-34608.
8. R. Silaghi-Dumitrescu, D. M. Kurtz, Jr., L. G. Ljungdahl and W. N. Lanzilotta, *Biochemistry*, 2005, **44**, 6492-6501.
9. A. Di Matteo, F. M. Scandurra, F. Testa, E. Forte, P. Sarti, M. Brunori and A. Giuffre, *J. Biol. Chem.*, 2008, **283**, 4061-4068.
10. A. J. Jasniewski and L. Que, Jr., *Chem. Rev.*, 2018, **118**, 2554-2592.
11. C. Frazao, G. Silva, C. M. Gomes, P. Matias, R. Coelho, L. Sieker, S. Macedo, M. Y. Liu, S. Oliveira, M. Teixeira, A. V. Xavier, C. Rodrigues-Pousada, M. A. Carrondo and J. Le Gall, *Nat. Struct. Biol.*, 2000, **7**, 1041-1045.
12. A. C. Rosenzweig, P. Nordlund, P. M. Takahara, C. A. Frederick and S. J. Lippard, *Chem. Biol.*, 1995, **2**, 409-418.
13. D. T. Logan, X. D. Su, A. Aberg, K. Regnstrom, J. Hajdu, H. Eklund and P. Nordlund, *Structure*, 1996, **4**, 1053-1064.
14. A. C. Weitz, N. Giri, R. E. Frederick, D. M. Kurtz, Jr., E. L. Bominaar and M. P. Hendrich, *ACS Catal.*, 2018, **8**, 11704-11715.
15. A. C. Weitz, N. Giri, J. D. Caranto, D. M. Kurtz, Jr., E. L. Bominaar and M. P. Hendrich, *J. Am. Chem. Soc.*, 2017, **139**, 12009-12019.
16. J. D. Caranto, A. Weitz, M. P. Hendrich and D. M. Kurtz, Jr., *J. Am. Chem. Soc.*, 2014, **136**, 7981-7992.
17. B. G. Fox, M. P. Hendrich, K. K. Surerus, K. K. Andersson, W. A. Froland, J. D. Lipscomb and E. Munck, *J. Am. Chem. Soc.*, 1993, **115**, 3688-3701.
18. J. B. Gordon, J. P. McGale, J. R. Prendergast, Z. Shirani-Sarmazeh, M. A. Siegler, G. N. L. Jameson and D. P. Goldberg, *J. Am. Chem. Soc.*, 2018, **140**, 14807-14822.
19. J. B. Lynch, C. Juarez-Garcia, E. Munck and L. Que, Jr., *J. Biol. Chem.*, 1989, **264**, 8091-8096.
20. T. Hayashi, J. D. Caranto, H. Matsumura, D. M. Kurtz, Jr. and P. Moenne-Loccoz, *J. Am. Chem. Soc.*, 2012, **134**, 6878-6884.

21. L. Lauterbach, L. B. Gee, V. Pelmenschikov, F. E. Jenney, S. Kamali, Y. Yoda, M. W. Adams and S. P. Cramer, *Dalton Trans.*, 2016, **45**, 7215-7219.
22. L. Lauterbach, H. X. Wang, M. Horch, L. B. Gee, Y. Yoda, Y. Tanaka, I. Zebger, O. Lenz and S. P. Cramer, *Chem. Sci.*, 2015, **6**, 1055-1060.
23. K. Park, T. Tsugawa, H. Furutachi, Y. Kwak, L. V. Liu, S. D. Wong, Y. Yoda, Y. Kobayashi, M. Saito, M. Kurokuzu, M. Seto, M. Suzuki and E. I. Solomon, *Angew. Chem. Int. Ed.*, 2013, **52**, 1294-1298.
24. N. Karthikeyan, J. J. Prince, S. Ramalingam and S. Periandy, *Spectrochim. Acta A Mol. Biomol. Spectrosc.*, 2015, **139**, 229-242.
25. J. Sandersloehr, W. D. Wheeler, A. K. Shiemke, B. A. Averill and T. M. Loehr, *J. Am. Chem. Soc.*, 1989, **111**, 8084-8093.
26. W. H. Armstrong, A. Spool, G. C. Papaefthymiou, R. B. Frankel and S. J. Lippard, *J. Am. Chem. Soc.*, 1984, **106**, 3653-3667.
27. A. C. Weitz, E. A. Hill, V. F. Oswald, E. L. Bominaar, A. S. Borovik, M. P. Hendrich and Y. S. Guo, *Angew. Chem. Int. Ed.*, 2018, **57**, 16010-16014.
28. L. Noodleman and D. A. Case, in *Adv. Inorg. Chem.*, ed. R. Cammack, Academic Press, 1992, vol. 38, pp. 423-470.

Supporting Information:

Hydroxo-bridged active site of a flavodiiron NO reductase revealed by spectroscopy and computations

Filipe Folgosa,[a,§] Vladimir Pelmenschikov,[b,*,§] Matthias Keck,[c] Christian Lorent,[b] Yoshitaka Yoda,[d] James A. Birrell,[e] Martin Kaupp,[b] Miguel Teixeira,[a] Kenji Tamasaku,[f] Christian Limberg,[c] Lars Lauterbach[b,*]

[a] *Instituto de Tecnologia Química e Biológica António Xavier, ITQB NOVA, Av. da República, 2780-157 Oeiras, Portugal*
[b] *Institut für Chemie, Technische Universität Berlin, 10623 Berlin, Germany. E-mail: lars.lauterbach@tu-berlin.de; pelmentschikov@tu-berlin.de*
[c] *Department of Chemistry, Humboldt-Universität zu Berlin, Brook-Taylor-Strasse 2, 12489 Berlin, Germany*
[d] *JASRI, SPring-8, Sayo-gun, Hyogo 679-5198, Japan*
[e] *Max Planck Institute for Chemical Energy Conversion, Stiftstrasse 34-36, 45470 Mülheim an der Ruhr, Germany*
[f] *RIKEN SPring-8 Center, Sayo-gun, Hyogo 679-5148, Japan*
* Corresponding authors.
§ These authors contributed equally.

Materials and Methods

Sample Preparation

The enzyme construct, FDP-D (residues 1 to 400 of the *norV* gene product, lacking the rubredoxin domain), was expressed as previously described.[1] To obtain ^{57}Fe enriched samples, the growth media was supplemented with 0.1 mM ^{57}FeCl both at the beginning of the growth and at the time of induction. The cells were disrupted by 3 cycles in a French press at 16000 psi (Thermo) in the presence of DNAse (Applichem) and the crude extract was clarified by low-speed centrifugation at 25,000 g for 25 min and at 138,000 g for 1 h and 30 min and at 4 °C to remove cell debris and the membrane fraction, respectively. The supernatant was dialysed overnight at 4 °C against 20 mM Tris–HCl, pH 7.5 containing 18% glycerol (buffer A). The soluble extract was then loaded onto a Q-Sepharose Fast-Flow column (50 mL, GE Healthcare) previously equilibrated with buffer A. FDP-D was eluted with a linear gradient from buffer A to 20 mM Tris–HCl, pH 7.5 containing 18% glycerol and 500 mM NaCl. The eluted fractions were analysed by 15% SDS-PAGE and UV–visible spectroscopy. Fractions containing pure protein were pooled and concentrated.

FDP-D sample was quantified and the iron and flavin content was evaluated as previously described.[2] The determined Fe/flavin/protein ratio was 2 (±0.2)/0.8 (±0.2)/1.

Reduced FDP-D samples used for NRVS, resonance Raman, and Mössbauer spectroscopy measurements were obtained anaerobically, inside a glovebox, by addition of a buffered sodium dithionite solution. Both as prepared and reduced samples were 2 mM in protein concentration.

Mössbauer Spectroscopy

Zero-field Mössbauer spectra were recorded on a SEECO MS6 spectrometer that comprises the following instruments: a JANIS CCS-850 cryostat, including a CTI-CRYOGENICS closed cycle 10 K refrigerator, and a CTI-CRYOGENICS 8200 helium compressor. The cold head and sample mount are equipped with calibrated DT-670-Cu-1.4L silicon diode temperature probes and heaters. The temperature was controlled by a LAKESHORE 335 temperature controller. Spectra were recorded using a LND-45431 Kr gas proportional counter with beryllium window connected to the SEECO W204 γ-ray spectrometer that includes a high voltage supply, a 10 bit and 5 µs

ADC and two single channel analysers. Motor control and recording of spectra was taken care of by the W304 resonant γ-ray spectrometer. For the reported spectra a RIVERTEC MCO7.114 source (^{57}Co in Rh matrix) with an activity of about 1 GBq was used. All spectra were recorded as frozen solutions at 13 K and data were accumulated for about 24 hours. Mössbauer data were processed and fitted using the WMOSS4 program (www.wmoss.org). Isomeric shifts are referenced to α-iron at room temperature.

Nuclear Resonance Vibrational Spectroscopy

Nuclear resonance vibrational spectroscopy (NRVS) measurements were performed at SPring-8 BL19LXU with a 0.8 meV energy resolution at 14.4125 keV as described previously.[3] A 2×2 elements avalanche photodiode detector array was used to detect delayed nuclear fluorescence and K fluorescence by ^{57}Fe atoms. All measurements were performed at a 10 K reading of the cryostat sensor. The real sample temperature, as obtained from the spectral analysis, was 30–80 K. To enhance the S/N ratio in the Fe-(OH)x-Fe range of the spectra, sectional measurements of these regions were performed. While for the usual scans the time for every point was 5 s, in the case of sectional scans the acquisition time for every data point in the region of interest, i.e. from 300 to 400 cm^{-1} was 8 s, from 600 to 800 cm^{-1} was 20 s, and for the remaining regions was 2 s. The raw data were analysed with the PHOENIX software to obtain the iron partial vibrational density of states (^{57}Fe-PVDOS).[4, 5]

Resonance Raman Spectroscopy

A LabRam HR-800 Jobin Yvon confocal Raman spectrometer coupled to a liquid-N_2-cooled charge-coupled device (CCD) was applied to accumulate resonance Raman spectra of pure FMN (2 mM and 50 mM potassium iodide at pH 8 in Tris-HCl buffer) and FDP samples (as described in the sample preparation section). The 458 nm or 514 nm emission lines of an Ar^+ ion laser beam at a power of 1-2 mW was focussed on a 2-4 µm spot on the surface of the sample drop to induce Raman scattering. The temperature was set to 80 K using a liquid-N_2-cooled cryo-stage (Linkam Scientific instruments). Toluene was used as an external standard for frequency calibration of each spectrum. Experimental data were analysed and processed using the Bruker OPUS software version 6.5 or higher.

Density Functional Theory Calculations

E. coli FDP oxidised active site topology employed in the present density functional theory (DFT) modelling was initially based on the crystal structure of *Moorella (M.) thermoacetica* FDP in its reduced and subsequently NO-reacted state, which corresponds to an oxidised sate (PDB 1YCH)[6] . This structure shows a bridging mono-oxo coordination in the active site. This selection of the X-ray reference based on a protein different from *E. coli* FDP is justified by (*i*) the absence of a co-crystallised species resolved in the active site of *M. thermoacetica* FDP, and (*ii*) otherwise very similar active site arrangements in the two enzymes as shown in Fig. S8. Upon adding protons, the extracted *M. thermoacetica* FDP active site coordinates were conveniently used as a starting structure for the representative FDP-D_{RED} state optimisation. Possible effects from either the phosphate anion coordination or the vacant bridging site, as resolved correspondingly in the active sites of as-isolated (oxidised) (PDB 4D02) or dithionite reduced (PDB 5LLD) *E. coli* FDP,[7] were investigated in this work separately. The model system involved only the protein side chains binding the Fe sites, terminating at C_α carbons, and saturating them with protons to methyl groups as shown in Fig. S10. At this modeling level, no conflicts are present between the aligned amino acid sequences of *E. coli* and *M. thermoacetica* FDPs. The amino acids entering the model are H79(81), E81(83), D83(85), H84(86), H147(148), D166(167), and H227(228), where the protein sequence numbers are respectively for *E. coli* FDP (*M. thermoacetica* FDP). All the seven C_α terminal carbon nuclei appearing in the above-described model were locked to their original positions in the X-ray crystallographic structures during structural optimisations and treated as frozen during normal mode analyses. Additionally, an alternative scheme including

fixation of the entire $-C_{\alpha}H_3$ methyl terminals has been investigated, as detailed below in Supplementary Results and Discussion, subsection (*viii*).

The DFT calculations were done mostly using GAUSSIAN 09 Revision D.01,[8] based on a high-quality initial guess from single point calculations using JAGUAR 9.4.[9] The qualified initial guess approach was specifically employed to ensure broken-symmetry (BS)[10] solutions, with electronic structures implying open-shell singlet states, unless otherwise mentioned. All the calculations employed the PBE0[11] hybrid functional in its spin-unrestricted formalism, and the LACV3P** basis set as implemented in JAGUAR 9.4. For the first- and second-row elements, LACV3P** implies 6-311G** triple-ζ basis sets including polarization functions. For the Fe atoms, LACV3P** consists of a triple-ζ basis set for the outermost core and valence orbitals, and the quasi-relativistic Los Alamos effective core potential (ECP) for the innermost electrons. The molecular systems environment was considered using a self-consistent reaction field (SCRF) polarizable continuum model and integral equation formalism (IEF-PCM),[12] with the static dielectric constant set to $\varepsilon = 4.0$ as often used for proteins, and the remaining IEF-PCM parameters at their default values for water. The calculations further included the two-body D3 dispersion corrections by Grimme et al.[13, 14] The ^{57}Fe-PVDOS and diatomic internuclear kinetic energy distribution (KED) intensities were extracted from GAUSSIAN 09 normal mode outputs using an in-house program Q-SPECTOR, successfully applied previously (e.g. in ref. 15) to simulate the spectra. To empirically account for the observed NRVS lineshape, the computed ^{57}Fe-PVDOS and KED intensities were broadened by Lorentzian convolution with a full width at half maximum (FWHM) = 14 cm^{-1}. An empirical scaling of the calculated frequencies was not applied.

Supplementary Results and Discussion

Alternative DFT Models

(*i*) Redox-dependent alternatives. Isomeric to the main FDP models with either mono- (μOH^-) or di- $(\mu OH^-)_2$ hydroxo bridging coordinations, a set of alternative DFT systems targeted redox-dependent effects at the three oxidation levels: Fe(II)Fe(II) reduced, Fe(II)Fe(III) mixed-valence (partially reduced), and Fe(III)Fe(III) oxidised. While no major transformations were produced upon the reduction level shifts in both structures (Fig. S11), the predicted ^{57}Fe-PVDOS spectra (Fig. S20) generally display notable variations as described below.

Our primary cross-check addressed the two structures with their oxidation levels interchanged. At the Fe(II)Fe(II) level, a dihydroxo differous system Fe(II)–$(\mu OH^-)_2$–Fe(II) produced strong conflicts to the observed FDP-D_{RED} spectrum (Fig. S20a) throughout the entire 0-600 cm^{-1} range, e.g. an absence of the ~580 cm^{-1} feature (attributed to the Fe(II)–μOH^- stretch in the monohydroxo system). At the Fe(III)Fe(III) level, a monohydroxo diferric system Fe(III)–(μOH^-)–Fe(III) is in lesser conflict with the FDP-D_{OX} NRVS data (Fig. S20c). With its (*i*) too sharp bands in the ~300-600 cm^{-1} and (*ii*) lack of intensity in the ~200-230 cm^{-1} regions, Fe(III)–(μOH^-)–Fe(III) is still inferior to the representative FDP-D_{OX} model. Notably, the Fe(III)–(μOH^-)–Fe(III) model produces prominent intensities at 543 cm^{-1} (Fe(III)–O(Glu81) stretch) and 585 cm^{-1} (Fe(III)–μOH^- stretch), not observed around the low-intensity high-end bands of the FDP-D_{OX} sample.

The mixed-valence Fe(III)Fe(II) states discourse a potential radiative $1e^-$ reduction of the FDP-D_{OX} sample under the NRVS experimental conditions with prolonged (>4 h) radiation exposure (see also Fig. S7). Among these S = 1/2 paramagnetic states, two alternatives (either 'Fe(II)Fe(III)' or 'Fe(III)Fe(II)') were computationally considered for each isomer, favouring by ~2-6 kcal/mol the solutions with the ferrous Fe(II) site coordinated by the Asp83 carboxylate. With their structures otherwise similar to those of the homovalent states, the mixed-valence solutions introduce enhanced asymmetry to the metal-hydroxo coordination, where the Fe(II)–μOH^- bonds become ~0.2 Å longer than the Fe(III)–μOH^- bonds. Here, the monohydroxo models Fe(II)–(μOH^-)–Fe(III)[S=1/2] and Fe(III)–(μOH^-)–Fe(II)[S=1/2] produce high-frequency Fe(III)–μOH^- stretches and associated ^{57}Fe-PVDOS bands at correspondingly 642 and 632 cm^{-1}, in conflict with the baseline intensity level in the 630-640 cm^{-1} area from the experiment (Fig. S20b). The dihydroxo models Fe(II)–$(\mu OH^-)_2$–Fe(III)[S=1/2] and Fe(III)–$(\mu OH^-)_2$–

Fe(II)[*S*=1/2] perform acceptably well in the higher energy area >300 cm^{-1}, yet these models do not contribute sufficient intensity close to the ~270 cm^{-1} global maximum of the representative FDP-D_{OX} spectrum (attributed to the Fe–N(His)/O(Asp,Glu) modes). To a lesser extent than in the reduced Fe(II)–$(\mu OH^-)_2$–Fe(II) model ^{57}Fe-PVDOS, the mixed-valence dihydroxo systems instead produce red-shifted global spectral maxima at vibrational energies below 220 cm^{-1}. Similar effects indicating partial photoreduction of the FDP-D_{OX} sample are seen upon longer (>4 h) NRVS collection intervals, in particular in the NRVS data collected after 16 h of the beam exposure (Fig. S7). Notably, following the Mössbauer spectroscopy results in Table S2, spectral simulation of the mixed-valence state employed in Figs. S7 and S20b included equal (50%) contributions from the two DFT models with either Fe site reduced, denoted as Fe(III)–$(\mu OH^-)_2$–Fe(II)[*S*=1/2]*.

(*ii*) Bridging hydroxyl interaction with Asp83 carboxylate. Upon a shift of the hydroxo ligand to its alternative 2nd bridging position as seen in the oxidised state Fe(III)–$(\mu OH^-)_2$–Fe(III) model, an isomeric reduced state model Fe(II)–(μOH^-)*–Fe(II) has been stabilised (Fig. S12). With its relative energy of +10 kcal/mol, the Fe(II)–(μOH^-)* –Fe(II) isomer lacks a favourable hydrogen bonding interaction between the hydroxo ligand and Asp83 carboxylate (O_{D1}), in contrast with the best-fit Fe(II)–(μOH^-)–Fe(II) model (μO(H)···O(Asp83) = 2.76 Å). Notably, as suggested by Fig. S8, short oxygen-to-oxygen μO···O(Asp) distances within 3 Å involving the homologous aspartate are available from the X-ray structures of *Ec* FDP (μO(H)···O(Asp83) = 2.63 Å, PDB 4D02[7]) and *M. thermoacetica* FDP (μO(H)···O(Asp85) ranges between 2.61 to 2.81 Å, PDB 1YCH[6]). The Fe(II)–(μOH^-)*–Fe(II) structure is reminiscent of a computational model of the *Thermotoga maritima* (*Tm*) FDP reduced state by Weitz et al,[16] which similarly avoids hydrogen bonding of a bridging mono-hydroxo ligand with the homologous aspartate (Asp89 in *Tm* FDP), albeit introducing an *in silico* rotation of the latter side chain. The optimised μO(H)···O(Asp83/89) = 3.8/3.4 Å distances were obtained in these two independent models of *Ec/Tm*FDP. With its markedly high relative energy, the Fe(II)–(μOH^-)*–Fe(II) model leads to ^{57}Fe-PVDOS largely inconsistent with the observed NRVS bands of FDP-D_{RED} (Fig. S21a). Specifically, due to a lack of the bridging hydroxo ligand polarisation (otherwise induced by interaction with Asp83), this model produces Fe–μOH^- bands red-shifted to ~480 and ~360 cm^{-1} *vs* their characteristic positions observed respectively at ~580 and ~420 cm^{-1}.

(*iii*) Electronic state alternatives. A complementary line of the DFT models, otherwise isomeric and isoelectronic to the best-fit ones, addressed an influence of the electronic state on the structures and predicted ^{57}Fe-PVDOS as shown in Figs. S12 and S21. All the DFT results described elsewhere in this work relied on broken-symmetry (BS)[10] solutions, implying antiferromagnetic coupling (antiparallel spin alignment) of the two Fe sites. Employing ferromagnetic coupling instead, systems Fe(II)–(μOH^-)–Fe(II)[*S*=4] (total spin *S* = 2 + 2 = 4) and Fe(III)–$(\mu OH^-)_2$–Fe(III)[*S*=5] (total spin *S* = 5/2 + 5/2 = 5) are high-spin (HS) equivalents of the representative reduced and oxidised FDP models. Fig. S21 displays very similar ^{57}Fe-PVDOS profiles for the structurally-optimised BS and HS equivalents, with at most only minor ~10 cm^{-1} deviations between the Fe–μOH^- band energies. Along with small calculated BS-to-HS electronic energy gaps within 2 kcal/mol, this result is indicative of a weak exchange coupling between the two Fe sites in FDP. The weak coupling predicted is additionally manifested in essentially unperturbed optimised structures of the HS solutions (Fig. S12). Additionally, an alternative BS solution $Fe(II)^{[S=1]}$–(μOH^-)–$Fe(II)^{[S=1]}$ (*S* = 1 - 1 = 0) for the reduced FDP model could be stabilised, where the Fe sites are intermediate-spin *S* = 1. This imaginary state, with its energy of approx. +50 kcal/mol and Fe–N(His)/O(Asp,Glu) bonds ~0.1 Å shorter relatively to the representative Fe(II)–(μOH^-)–Fe(II) model, fails to reproduce the experimental spectrum even remotely well.

(*iv*) Vacant bridging site and protonation alternatives. A set of alternative structural models of the FDP active site has been further explored computationally, based on either the bridging hydroxo ligands elimination or their protonation level changes, as compared to the best-fit Fe(II)–(μOH^-)–Fe(II) reduced and Fe(III)–$(\mu OH^-)_2$–Fe(III)

oxidised models. The structures of these models and their ^{57}Fe-PVDOS spectra are shown respectively in Figs. S13 and S22.

Systems named Fe(II)–( )–Fe(II) and Fe(III)–( )–Fe(III) with the bridging ligand sites vacant produce increased Fe···Fe separation distances, and spectral signatures clearly different from the experimental NRVS data. Notably, the Fe(II)–( )–Fe(II) configuration, although consistent with the structure of the reduced *E. coli* FDP PDB 5LLD[7] (Fig. S8), can be ruled out as a major species of the FDP-D_{RED} NRVS sample (see additional notes on a Fe(II)–( )–Fe(II)(O_2)[*S*=1] model below).

Bridging oxo (oxygen dianion) systems Fe(II)–(μO^{2-})–Fe(II) and Fe(III)–(μOH^-)(μO^{2-})–Fe(III) correspond to singly deprotonated systems, and produce intense Fe–μO^{2-} bands in the ~500-710 cm^{-1} region, absent at these jointly high intensities and vibrational energies from the NRVS data. An attempt to stabilise a water ligand bridge in the reduced state corresponds to a singly protonated model and results in proton transfer from H_2O towards the Asp83 carboxylate, where the latter loses its metal coordination (Fe···O(Asp83) = 2.44 Å), in a system called Fe(II)–(μOH^-)–Fe(II)(D83H$^+$). This model produces its Fe–μOH^- band ~50 cm^{-1} red-shifted compared to the high-end feature of the FDP-D_{RED} spectrum at 581 cm^{-1}.

(*v*) Variable dioxygen species. Yet another set of the DFT models featured dioxygen species at the FDP active site as shown in Fig. S14, with their corresponding ^{57}Fe-PVDOS spectra in Fig. S23. Structural optimisation of a doubly deprotonated (*vs* the best-fit oxidised state model) di-oxo Fe(III)–(μO^{2-})$_2$–Fe(III) system leads instead to an internal redox process and an O–O bond formation in a doubly-bridging peroxo diferrous model called Fe(II)–(μO_2^-)–Fe(II), with its sharp Fe–μO_2 band at ~400 cm^{-1}. Further, an attempt to stabilise the molecular oxygen in a bridging position between the two reduced metal sites, Fe(II)–(μO_2)–Fe(II)[*S*=1], leads instead to a semi-bridging superoxo state Fe(III)–($\mu O_2^{\bullet-}$)···Fe(II)[*S*=1]. The latter model is however 4 kcal/mol less favourable (electronic energy; 7.5 kcal/mol less favourable when the free energies are considered) as compared to its isomer, a Fe(II)–( )–Fe(II)(O_2)[*S*=1] model where the molecular oxygen is discharged from the bridge and placed initially following the O_2 coordinates resolved in the structure of the reduced *E. coli* (PDB 5LLD[7]) (Figs. 1 (B) and S8). A local minimum for the weakly bound O_2 molecule was therefore obtained with the shortest optimised Fe···O separation distances to the two iron sites of 3.5/3.7 Å, somewhat longer than 2.6/3.4 Å as found in PDB 5LLD. The ^{57}Fe-PVDOS signature of the Fe(II)–( )–Fe(II)(O_2)[*S*=1] model (Fig. S23) is apparently similar to that of the Fe(II)–( )–Fe(II) model (Fig. S22a). In summary, while the above-considered dioxygen species spectra are not reminiscent to any of the presently collected FDP-$D_{RED/OX}$ NRVS data, these results are relevant to the chemistry by FDPs, which often display both O_2 and NO reductase activities.

(*vi*) Phosphate anion coordination. Potential occupancy of the FDP active site by a phosphate anion, resolved in the as-isolated (oxidised) *E. coli* FDP (PDB 4D02)[7] structure additionally to the mono hydroxo bridge (Fig. S8), was investigated in alternative DFT models shown in Fig. S15 with their computed ^{57}Fe-PVDOS spectra in Fig. S24. The highly negative and bulky PO_4^{3-} species are likely to introduce extra interactions with the active site environment (as compared to e.g. hydroxo ligands) not explicitly available in the present DFT setup. To partially account for such interactions, models with the protonated PO_4H^{2-} species were considered as well. The latter protonated form of the phosphate anion as well better corresponds to the physiologic pH levels. The two oxidised state models Fe(III)–(μOH^-)–Fe(III)(PO_4H^{2-}) and Fe(III)–(μOH^-)–Fe(III)(PO_4^{3-}) overlap very well with the experimental X-ray structure (Fig. S15 bottom); the Fe–O(PO_4H^{2-}) / Fe–O(PO_4^{3-}) = 1.90-1.93 / 1.83-1.85 Å distances slightly favour the protonated PO_4H^{2-} modeling, when compared to the corresponding values of 1.9 and 2.3 Å as found in PDB 4D02. At the same time, phosphate coordination to the reduced FDP state in models Fe(II)–(μOH^-)–Fe(II)(PO_4H^{2-}) and Fe(II)–(μOH^-)–Fe(II)(PO_4^{3-}) (Fig. S15 top) is concluded to induce critical active site perturbations, such as Fe–O(Asp)/N(His) protein ligands loss. Among the phosphate-containing oxidised state models, Fe(III)–(μOH^-)–Fe(III)(PO_4H^{2-}) produces a more realistic ^{57}Fe-PVDOS spectra. However, similarly to another mono-hydroxo model Fe(III)–(μOH^-)–Fe(III) described above, it shows intensity drop-down in the ~200-230 cm^{-1} region and also around

~400 cm^{-1}, now less consistent with the FDP-D_{OX} spectrum (Fig. S24b). The phosphate-dependent normal modes yielding noticeable ^{57}Fe-PVDOS intensities in this model are O–P–O bends, coupled to either the Fe(III)–μOH^- stretches at 511 and 484 cm^{-1}, or to the Fe–O(PO_4H^{2-}) symmetric stretch at 432 cm^{-1}.

***(vii)* Bridging hydroxyl interaction with a solvent water molecule.** Following an earlier iron-oxido/hydroxido ^{57}Fe-NRVS and DFT study,[17] an importance of hydrogen bonding interactions to the iron-bound hydroxo ligand has been presently examined by inclusion of a solvent water molecule as found in the FDP active site pocket of, e.g., the reduced state of *M. thermoacetica* FDP (Fig. S8). The corresponding DFT models Fe(II)–(μOH^-)–Fe(II)(H_2O) and Fe(III)–$(\mu OH^-)_2$–Fe(III)(H_2O) are shown in Fig. S16, with their predicted ^{57}Fe-PVDOS spectra in Fig. S25. The $\mu O(H)\cdots O(H_2O)$ = 2.8-2.9 Å (oxygen-oxygen nuclei) distance remains essentially unaltered between the PDB 1YCH[6] X-ray reference and the optimised structures, supportive of the protonation scenario from the present modeling. The weakly bound H_2O molecule however forms additional (Asp166/Glu81)O$\cdots$H(H_2O) hydrogen bonds to the metal-bound carboxylates upon structure optimisations, which are possibly artefacts in the absence of other protein side chains forming the FDP active site pocket. Several characteristic Fe–μOH^- bands > 400 cm^{-1} become unfavourably red-shifted by 20-30 cm^{-1} in the Fe(II)–(μOH^-)–Fe(II)(H_2O) and Fe(III)–$(\mu OH^-)_2$–Fe(III)(H_2O) models. The *implicit* solvent SCRF / IEF-PCP scheme otherwise employed here, in contrast to the *explicit* H_2O inclusion, is therefore empirically concluded to serve as an optimal approach.

***(viii)* Rigid protein backbone scheme.** In view of notable displacements of the Fe-coordinating residues obtained for some of the models described above, a rigid ("[*R*]") protein backbone framework scheme has been alternatively explored in models Fe(II)–(μOH^-)–Fe(II)[*R*] and Fe(III)–$(\mu OH^-)_2$–Fe(III)[*R*] shown in Fig. S17, with their predicted ^{57}Fe-PVDOS spectra in Fig. S26. In contrast to the C_α-only fixation scheme permitting rotations of the side chains, such rotations are severely restricted when the entire $-C_\alpha H_3$ methyl terminal fixations are imposed. Alternative side chain to backbone fixation schemes have been previously examined in DFT modeling of ^{57}Fe-NRVS spectra of e.g. the methane monooxygenase binuclear iron site[18] and protein [4Fe-4S] clusters.[15] Interestingly, the rigid backbone scheme results in an over-extended (Asp166)O$\cdots$Fe = 2.8 Å distance in the reduced state structure, implying the bidentate Asp166 coordination lost to one of the Fe sites (Fig. S17). In contrast, all three X-ray structures collected in Fig. S8 and the reduced/oxidised representative models from the C_α-only fixation scheme show the (Asp166)O–Fe = 2.1-2.2 Å distance within its bonding range. The (Asp166)O–Fe coordination loss in the Fe(II)–(μOH^-)–Fe(II)[*R*] model can be rationalised by positioning of the His148 residue in the *M. thermoacetica* FDP PDB 1YCH[6] X-ray reference, which coordinates to the same Fe site; in the rigid backbone DFT model, the His148 imidazole displacement is restricted and the favourable Fe coordination to both the His148 imidazole and Asp166 carboxylate cannot be achieved. The His148 position notably different to that of PDB 1YCH[6] is seen in both the *E. coli* FDP structures (Figs. S8) and the representative DFT models (Fig. S9). While the reduced state Fe(II)–(μOH^-)–Fe(II)[*R*] model produces its characteristic high-frequency band ~50 cm^{-1} blue-shifted (Fig. S26a) as compared to that from the representative model and the FDP-D_{RED} NRVS data (570-580 cm^{-1}), the oxidised state rigid backbone model Fe(III)–$(\mu OH^-)_2$–Fe(III)[*R*] does not lead to the (Asp166)O–Fe coordination loss and performs on ^{57}Fe-PVDOS well in line with the experimental results (Fig. S26b); above 300 cm^{-1}, the performance of Fe(III)–$(\mu OH^-)_2$–Fe(III)[*R*] is somewhat superior to the otherwise representative Fe(III)–$(\mu OH^-)_2$–Fe(III) model. In summary, the common 'soft backbone' C_α-only fixation scheme was found optimal for a multi-state modeling of the FDP active site.

Mössbauer Spectroscopy of a Photoreduced State

Mössbauer spectra recorded after the NRVS measurements (Fig. S5) revealed two new additional iron species with a total of 12% contribution (Table S2) with parameters corresponding to high-spin Fe^{2+}, which indicates partial photoreduction by the 14.4 keV X-rays. Assuming reduction of only one out of two Fe centres per active site, 12% Fe^{2+} couples to 12% Fe^{3+} in a mixed-valence state. This provides 24% contribution of the signal assigned

to the photoreduced state. Following analysis in subsection (*i*) above and in the main text, photoreduction of the FDP-D_{OX} sample to a fully reduced diferrous species is a less likely alternative.

Table S1 Overview of Mössbauer parameters and bridging/terminal ligands at the active site of non-haem diiron enzymes. δ = isomer shift, ΔE_Q = quadrupole splitting. The oxidised Fe(III)Fe(III) (upper section) and reduced Fe(II)Fe(II) (lower section) enzyme states are augmented with notations 'ox' and 'red', respectively.

Enzyme	Fe Ligand(s)	δ (mm/s)	ΔE_Q (mm/s)	Ref.
Fe(III)Fe(III):				
FDP-D_{OX} *E.coli*	bis(μ-OH^-) [a]	0.50, 0.49	0.73, 1.03	this study
FDP-ox *T. maritima*	bis(μ-OH^-) [a]	0.48, 0.43	1.04, 0.94	16
deflavo-FDP-ox *T. maritima*	bis(μ-OH^-) [a]	0.44	0.92	16
oxy-haemerythrin	OOH^-, μ-O^{2-} [a, b, c]	0.46, 0.47	1.87, 0.94	19-22
sMMO-ox	bis(μ-OH^-) [b]	0.50	1.07	23, 24
ribonucleotide reductase-ox	μ-O^{2-}, 2 H_2O [b]	0.55, 0.45	-1.62, -2.44	25, 26
toluene-4-monooxygenase	μ-OH^-, μ-thioglycolate H_2O [b]	0.51, 0.56	0.93, 1.55	27, 28
Fe(II)Fe(II):				
FDP-D_{RED} *E.coli*	μ-OH^- [a]	1.18, 1.20, 1.31	2.16, 2.51, 3.23	this study
$Fe(H_2O)_6$		1.39	3.38	29
FDP_{red} *T. maritima*	μ-OH^- [a]	1.15	+2.39	16
deflavo-FDP_{red} *T. maritima*	μ-OH^- [a]	1.15	+2.5	16
deoxy-haemerythrin	μ-OH^- [b]	1.15	2.80	19-22
$sMMO_{red}$	μ-OH^-, μ-COO^- [d, b]	1.30	3.14, 2.4	23, 24, 30
ribonucleotide reductase-red	μ-COO^- [e, b]	1.26	3.13	25, 31
toluene-4-monooxygenase	n.a.*	1.31	3.21, 2.68	28

* Structure is not available.
[a] Spectroscopic evidence.
[b] Crystal structure.
[c] Computational evidence.
[d] Glu243 bidentate, additional to Glu144.
[e] Glu238 bidentate, additional to Glu115 (amino acid numbering from *E. coli* R2 RNR).

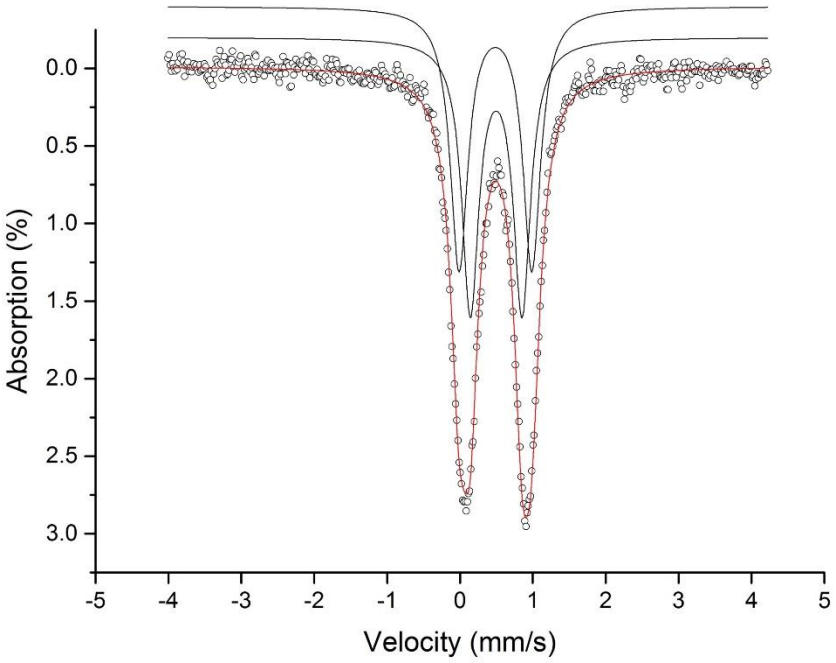

711

712

713 **Fig. S1** Mössbauer spectrum for FDP-D_{OX}. Solid lines on top of experimental spectra represent the different fitted
714 species (Tables 1 and S2). The empty circles are the experimental data, the red line is the global fit, and the black
715 lines indicate the component subspectra. Extended Mössbauer data collection of FDP-D_{OX} (3 days) show constant
716 peak positions (not shown), indicating no radiation damage by the applied ^{57}Co source.

717

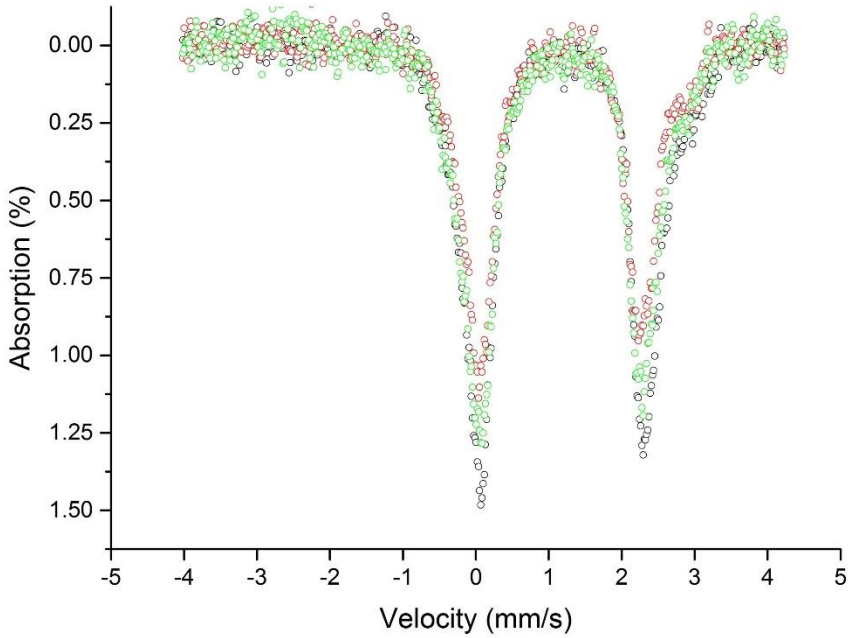

718 **Fig. S2** Mössbauer spectra of the FDP-D_{RED} sample at 13 K (black circles), at 120 K (red circles), both in the absence
719 of an applied magnetic field, and at 13 K with a magnetic field of 37 mT applied parallel to the γ-ray direction
720 (green circles).

721 **Fig. S3** Mössbauer subspectra of FDP-D_{RED} (experimental: empty circles, global fit: solid red line). Solid black lines
722 on top of experimental spectra represent the component subspectra (Tables 1 and S2).

723

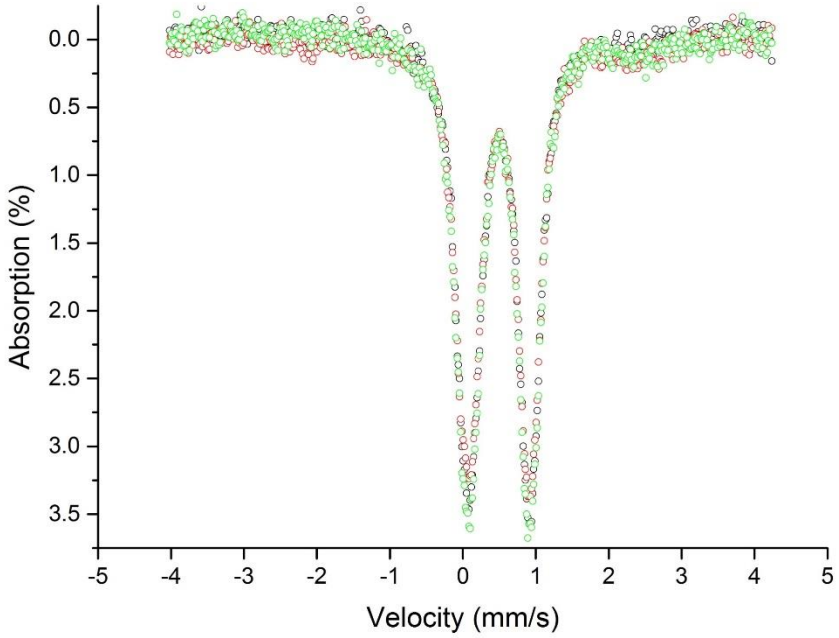

724 **Fig. S4** Zero-field Mössbauer spectra of the FDP-D_{OX} NRVS sample after 4 h (black dots), 6 h (red dots) and 10 h
725 (green dots) of NRVS irradiation.

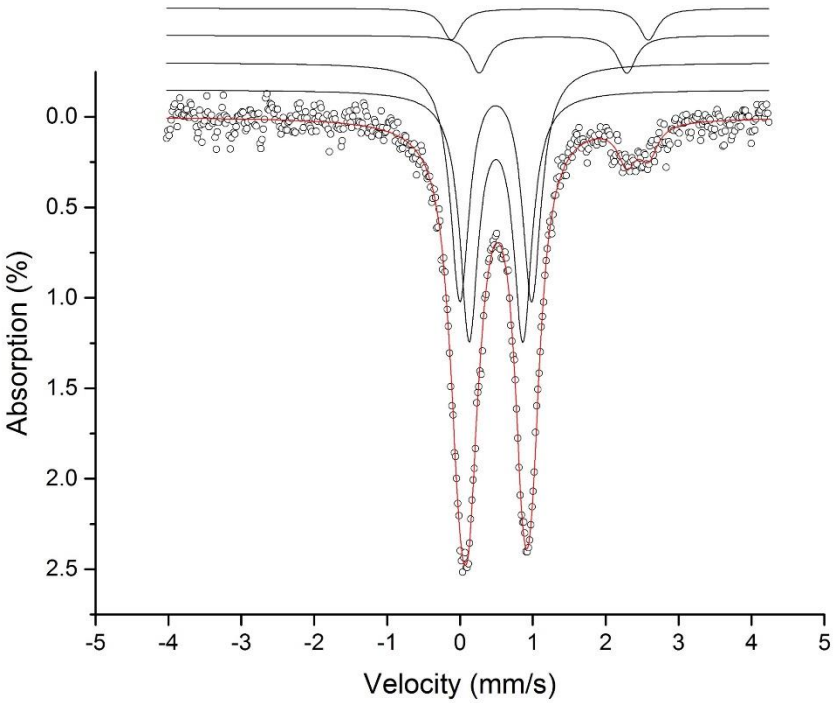

Fig. S5 Zero-field Mössbauer spectrum (experimental: black dots, simulation: red line) of FDP-D_{OX} sample after 20 h of NRVS measurement. Solid lines on top of experimental spectrum represent different simulated species listed in Table S2.

Table S2 Mössbauer parameters of FDP-D_{OX} sample after 20 and 10 h of NRVS irradiation in comparison to FDP-D_{OX} and FDP-D_{RED} before NRVS. δ = isomer shift, ΔE_Q = quadrupole splitting, Γ = line width at half maximum, I = intensity contribution, h.s. = high spin.

Sample	Species			δ (mm/s)	ΔE_Q (mm/s)	Γ (mm/s)	I (%)
FDP-D_{OX} After 20h NRVS	#1	Fe^{3+}	h.s.	0.50	0.74	0.30	44
	#2	Fe^{3+}	h.s.	0.49	0.99	0.32	44
	#3	Fe^{2+}	h.s.	1.28	2.03	0.30	6.5
	#4	Fe^{2+}	h.s.	1.24	2.70	0.30	5.5
FDP-D_{OX} After 10h NRVS	#1	Fe^{3+}	h.s.	0.50	0.72	0.27	47
	#2	Fe^{3+}	h.s.	0.49	0.98	0.28	47
	#3	Fe^{2+}	h.s.	1.25	2.00	0.3	3.5
	#4	Fe^{2+}	h.s.	1.22	2.79	0.3	2.5
FDP-D_{OX} Before NRVS	#1	Fe^{3+}	h.s.	0.50	0.71	0.28	50
	#2	Fe^{3+}	h.s.	0.49	1.00	0.29	50
FDP-D_{RED} Before NRVS	#1	Fe^{2+}	h.s.	1.18	2.14	0.29	43.5
	#2	Fe^{2+}	h.s.	1.20	2.46	0.38	43.5
	#3	Fe^{2+}	h.s.	1.32	3.23	0.44	13

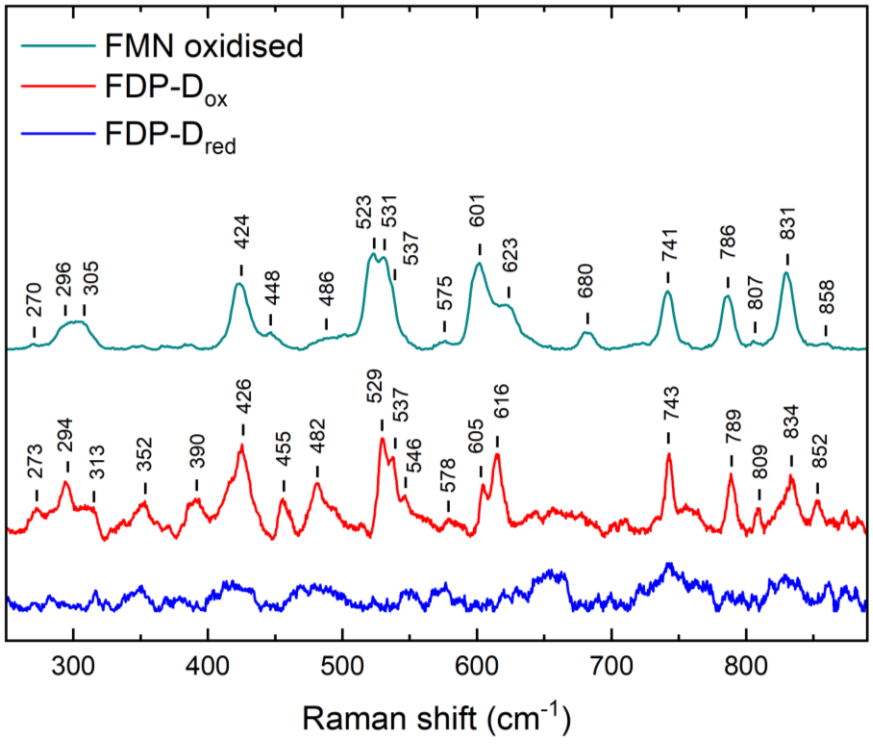

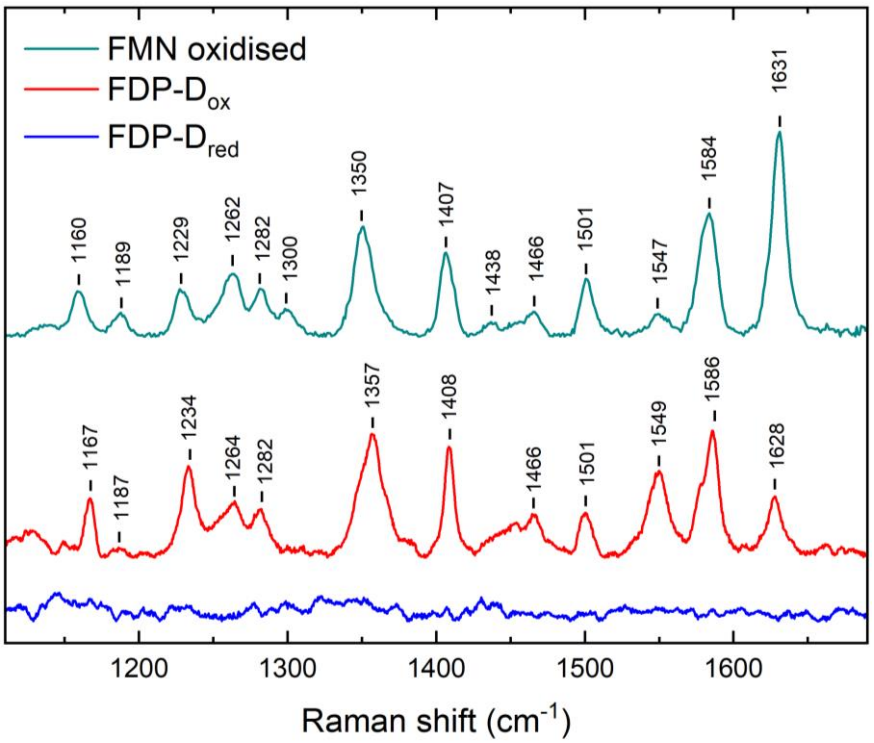

Fig. S6 Resonance Raman (RR) spectra of oxidised FMN (dark cyan), oxidised (red) and reduced (blue) FDP-D in the low- (top panel) and high-frequency (bottom panel) ranges. Spectra were recorded at 80 K using 458 nm (for pure FMN) and 514 nm laser excitation for FDP-D characterisation. While the RR spectra of oxidised and reduced FDP-D are normalised to the non-resonant marker band of phenylalanine at 1004 cm^{-1}, the spectrum of pure FMN is normalised with respect to the most intense signals at 529/523 cm^{-1} (top panel) and 1357/1350 cm^{-1} (bottom panel) in oxidised FDP-D. Variations of the relative signal intensities may correspond to the different

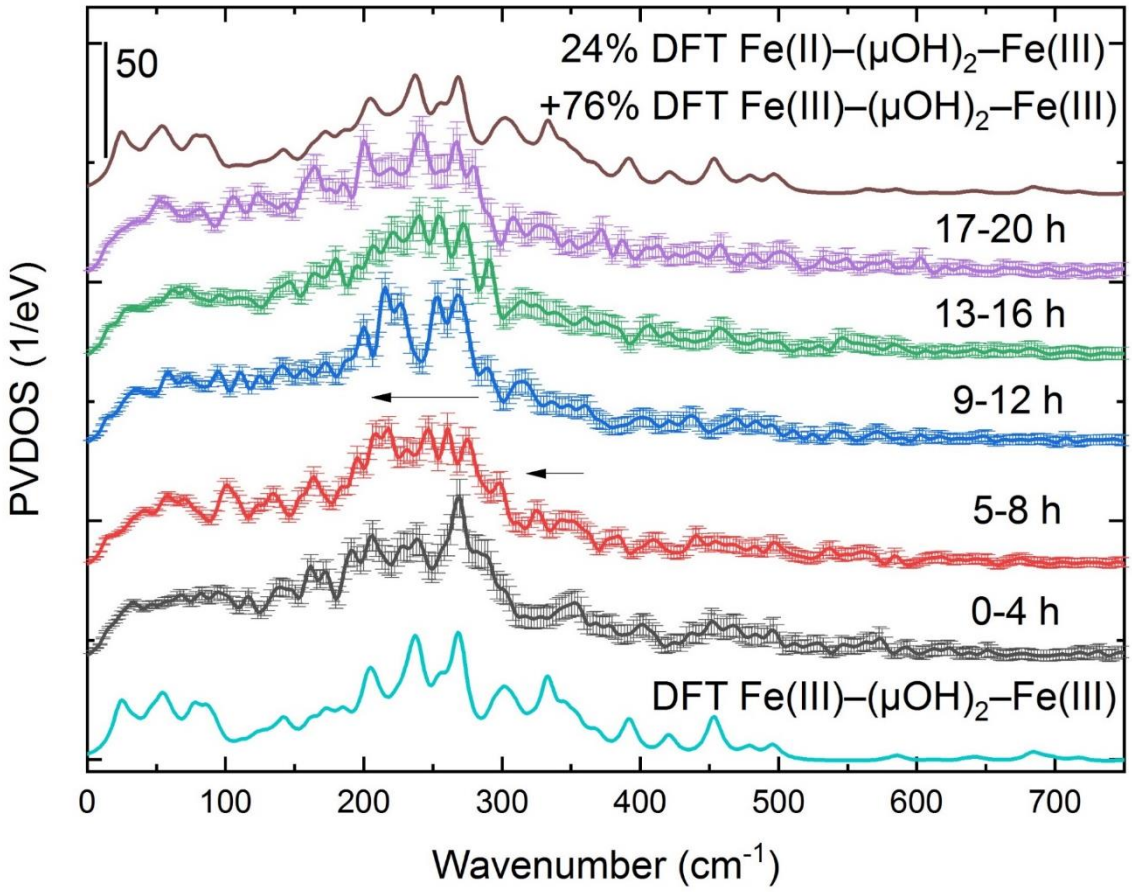

energies used for laser excitation. Small shifts of the band positions are most likely related to the environmental differences between free and enzyme-bound FMN.

Fig. S7 NRVS spectra of FDP-D_{OX} obtained after various intervals of data collection. ^{57}Fe-PVDOS were calculated from spectra obtained during consecutive 4 h intervals of the data collection and are presented with standard deviations. As every individual scan was obtained in 1 h, each of the spectra shown collects data from 4 scans. DFT-simulated spectra from the representative FDP-D_{OX} model Fe(III)–$(\mu OH^-)_2$–Fe(III) (bottom) and 24% contribution of the mixed-valence model Fe(III)–$(\mu OH^-)_2$–Fe(II)[*S*=1/2]* (top) are shown next to the spectra of FDP-D_{OX} (0-4 h) and partial photoreduced (17-20 h) species, respectively (see Fig. S5 and Table S2 for more details). A DFT-simulated spectrum for the pure (100%) mixed-valence state Fe(III)–$(\mu OH^-)_2$–Fe(II)[*S*=1/2]* (as explained in the Supplementary Results and Discussion subsection (*i*)) is found in Fig. 20b. Arrows indicate changes of spectra upon additional 4 hours of the X-ray photoreduction process. The first 4 scans of this sample (0-4 h) and additionally the first 4 scans of three other samples were used for calculating the averaged ^{57}Fe-PVDOS of FDP-D_{OX} shown in Fig. 3 bottom.

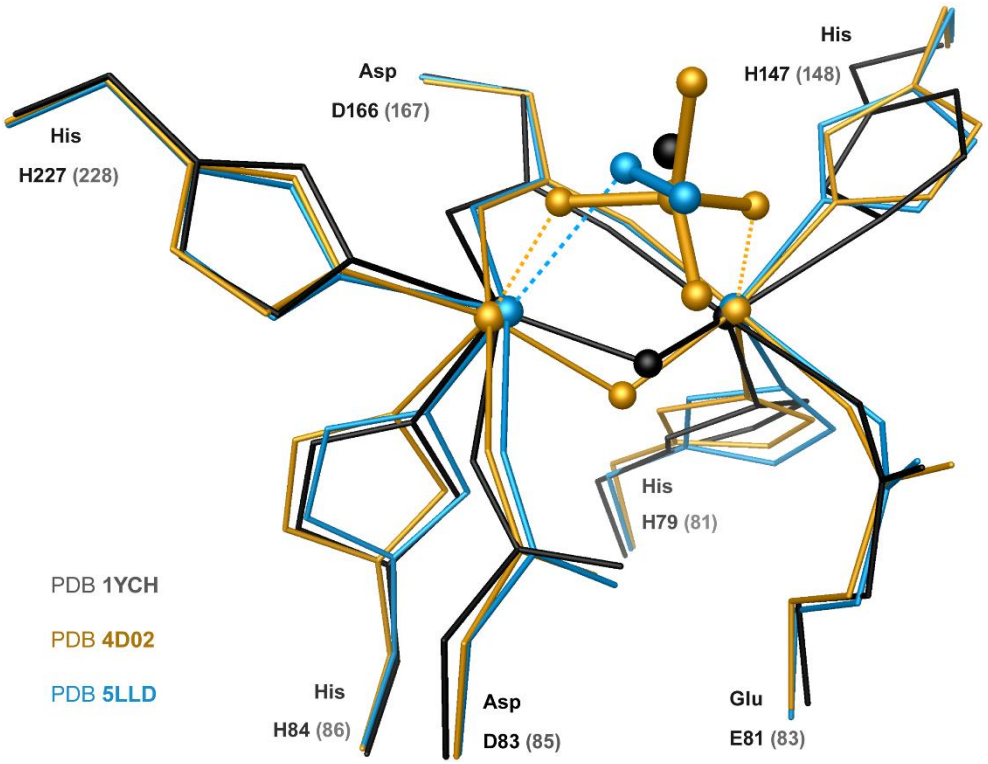

765

766

767 **Fig. S8** Crystallographic structures of the FDP active site from the *E. coli* enzyme as-isolated (beige, PDB 4D02[7])
768 and dithionite-reduced (blue, PDB 5LLD[7]) forms, superimposed onto the structure of the *M. thermoacetica*
769 enzyme reduced and NO-reacted form (which correspond to a diferric species, black, PDB 1YCH[6]) using positions
770 of the seven matching terminal C_α carbon nuclei from the Fe-binding residues. The corresponding RMSD values
771 for the matching C_α positions after the superposition are 0.194 (4D02 vs 1YCH) and 0.219 (5LLD vs 1YCH) Å. The
772 ball-and-stick representation applies to the two Fe sites and non-protein molecular species resolved in their
773 vicinity (mono-, di-oxygenous species, and phosphate). The amino acid numbering shown corresponds to the
774 sequences of FDPs from *E. coli* (*M. thermoacetica*).

775

776

777

778

779

780

781

782

783

784

785

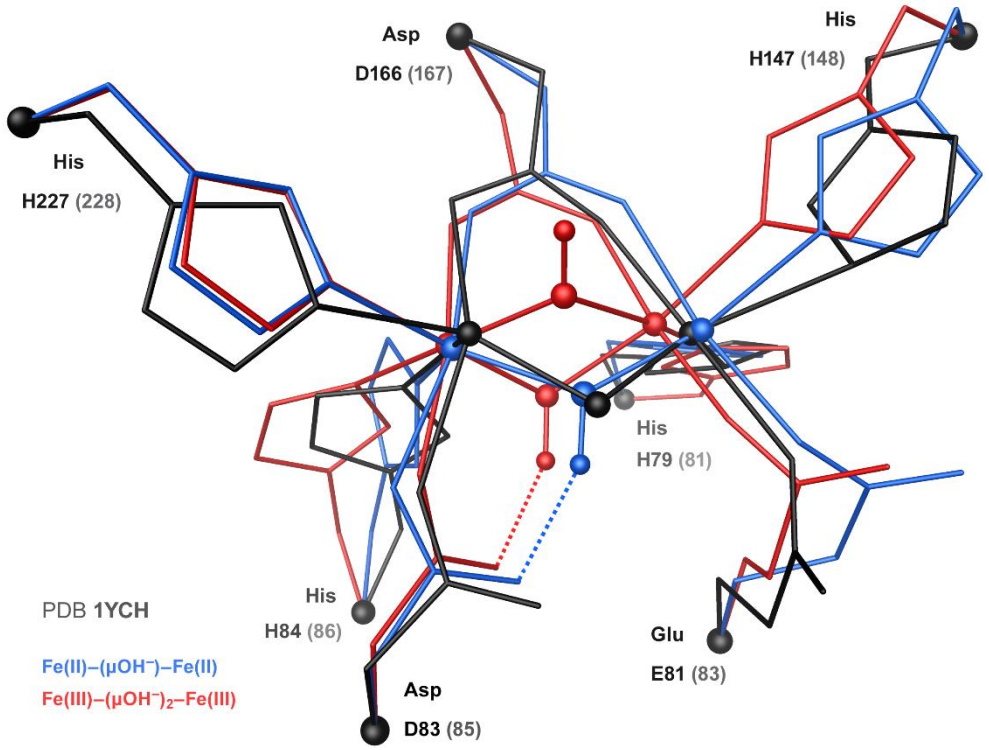

Fig. S9 Representative DFT-optimised models of the FDP reduced Fe(II)–(μOH$^-$)–Fe(II) (blue) and oxidised Fe(III)–(μOH$^-$)$_2$–Fe(III) (red) states, overlaid with crystallographic structure of the *M. thermoacetica* FDP (PDB 1YCH[6]) (black). For clarity, protonation is shown only for the bridging μOH$^-$ ligands, which are depicted in the ball-and-stick representation. The ball-and-stick representation applies also to the two Fe sites and seven C_α (black) terminal carbon nuclei. The latter were fixed to their original X-ray crystallographic positions. The amino acid numbering shown corresponds to the sequences of FDP from *E. coli* (*M. thermoacetica*).

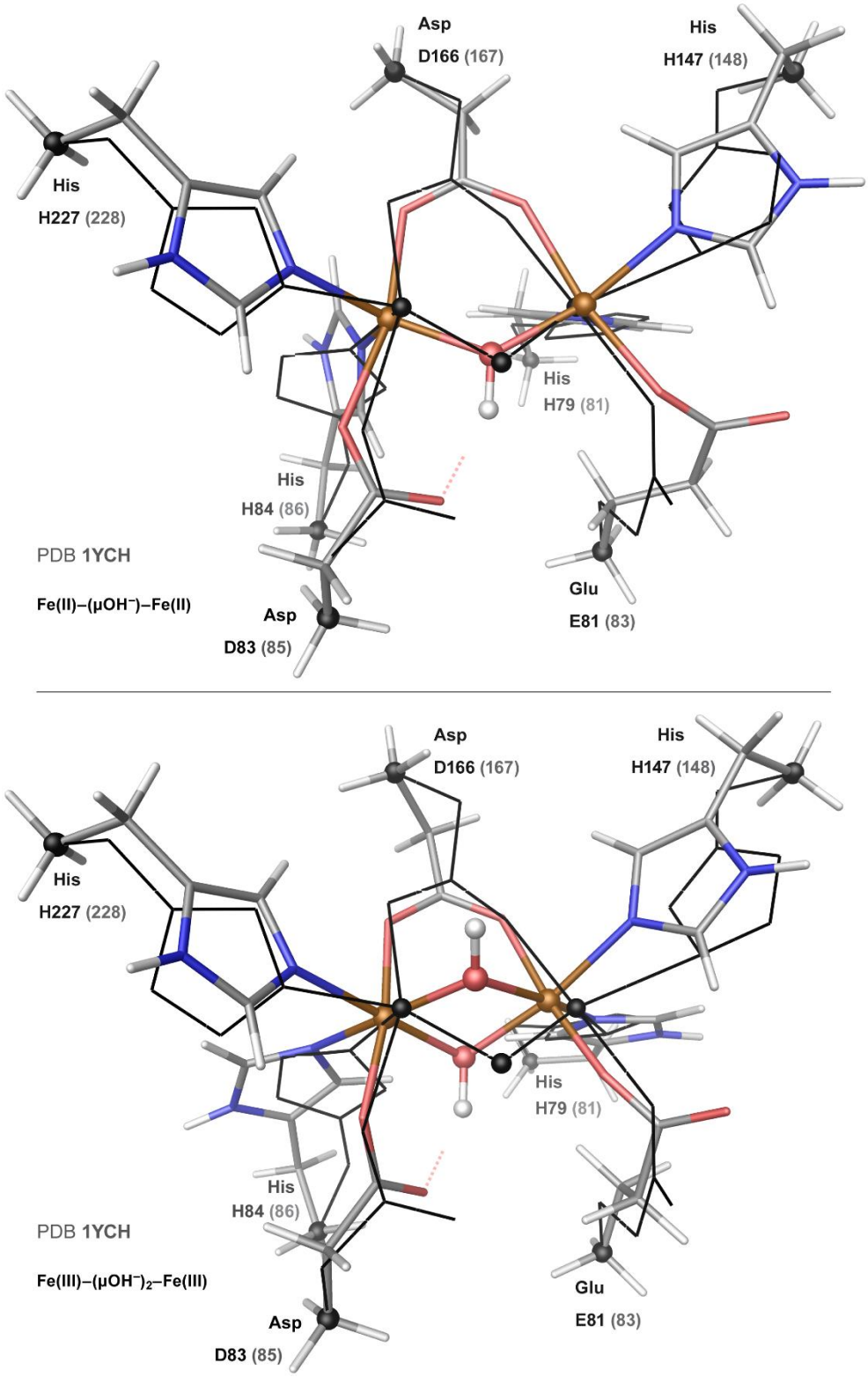

Fig. S10 Representative DFT-optimised models of the FDP active site in the reduced Fe(II)–(μOH$^-$)–Fe(II) (top) and oxidised as-isolated Fe(III)–(μOH$^-$)$_2$–Fe(III) (bottom) states (element colors, tube representation), overlaid with the X-ray crystal structure of the *M. thermoacetica* FDP (PDB 1YCH,[6] black, wire representation). The bridging μOH$^-$ ligands and the two Fe sites are depicted in ball-and-stick representation. This representation applies also to the seven C_α terminal carbon nuclei (black), which were fixed to their original X-ray crystallographic positions. The amino acid numbering shown corresponds to the sequences of FDP from *E. coli* (*M. thermoacetica*).

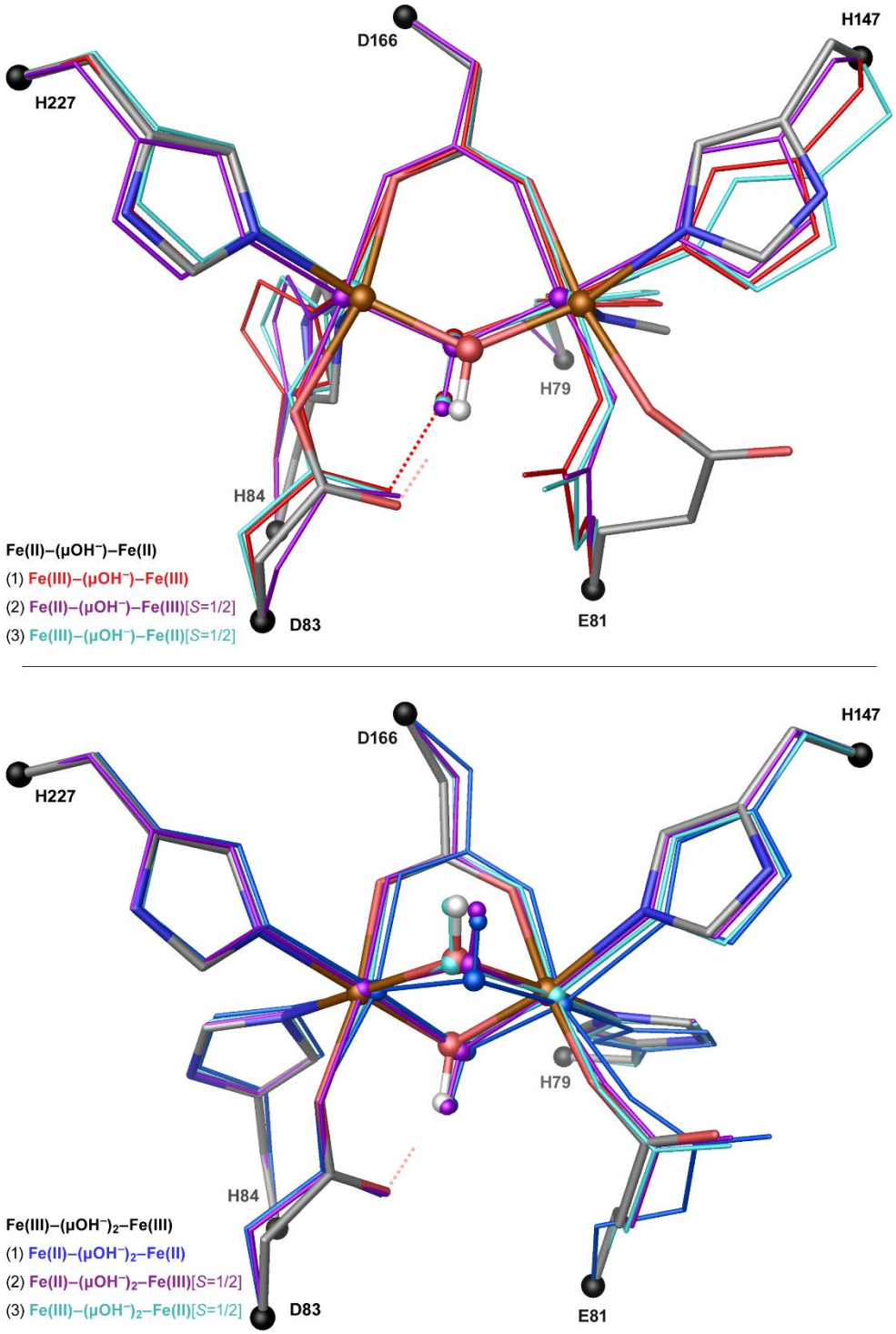

Fig. S11 Representative Fe(II)–(μOH$^-$)–Fe(II) (top) and Fe(III)–(μOH$^-$)$_2$–Fe(III) (bottom) DFT models of the FDP active site (element colors, tube representation), overlaid together with isomeric (but not isoelectronic) structures at alternative metal oxidation levels (thin tubes). Top: (**1**) Fe(III)–(μOH$^-$)–Fe(III) (red), (**2**) Fe(II)–(μOH$^-$)–Fe(III)[*S*=1/2] (violet), (**3**) Fe(III)–(μOH$^-$)–Fe(II)[*S*=1/2] (cyan). Bottom: (**1**) Fe(II)–(μOH$^-$)$_2$–Fe(II) (blue), (**2**) Fe(II)–(μOH$^-$)$_2$–Fe(III)[*S*=1/2] (violet), (**3**) Fe(III)–(μOH$^-$)$_2$–Fe(II)[*S*=1/2] (cyan). For the mixed-valence Fe(II)Fe(III) and Fe(III)Fe(II) systems, the metal oxidation levels are consistently left-to-right both in the model nomenclatures and structures shown. For clarity, the protonations are shown only for the bridging μOH$^-$ ligands, which are depicted in ball-and-stick representation. The ball-and-stick representation applies as well to the two Fe sites and seven C$_\alpha$ (black) terminal carbon nuclei, the latter locked to their original X-ray crystal structure positions.

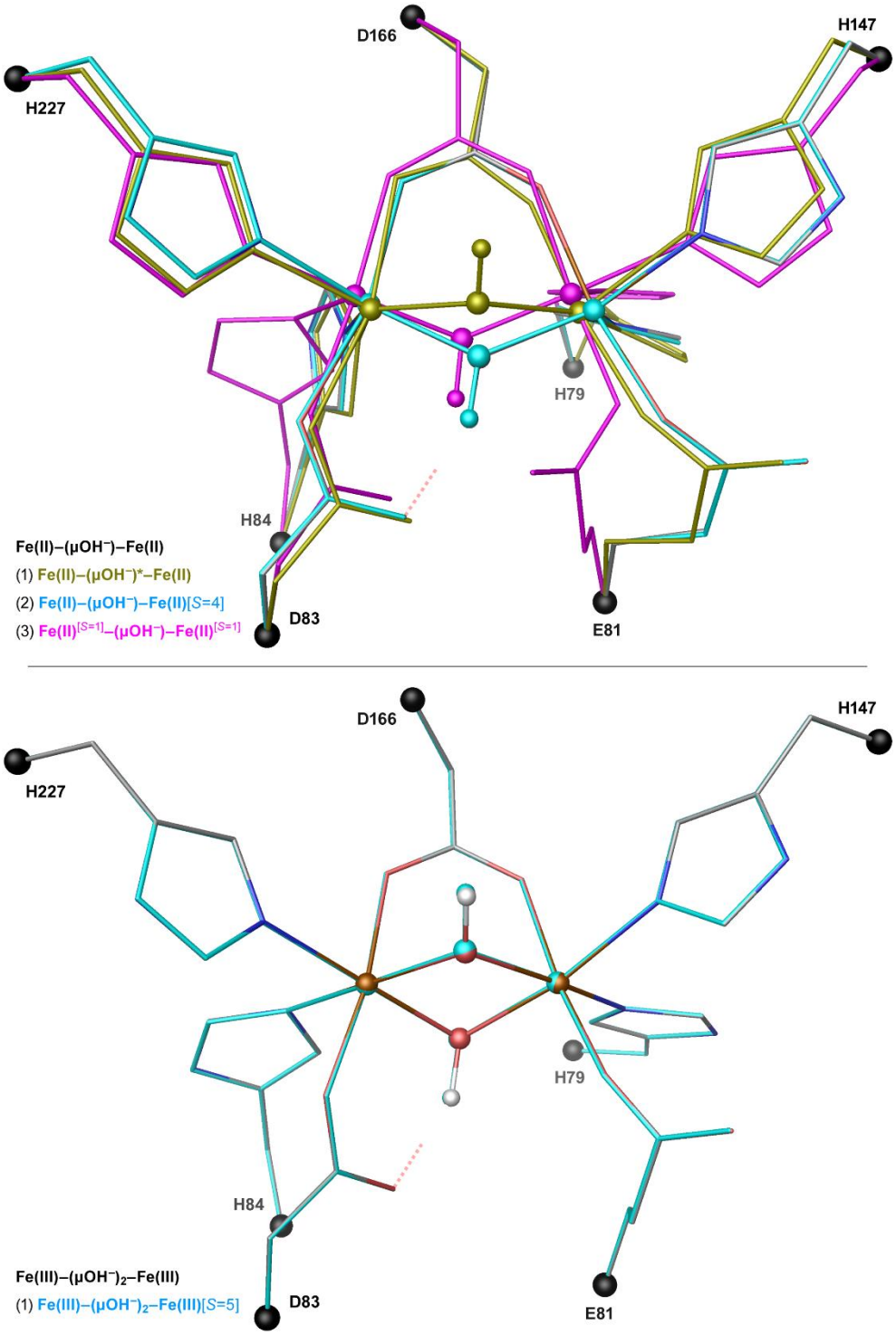

Fig. S12 Representative Fe(II)–(μOH$^-$)–Fe(II) (top) and Fe(III)–(μOH$^-$)$_2$–Fe(III) (bottom) DFT models of the FDP active site (element colors, thin tube representation), overlaid together with isomeric (and isoelectronic) structures at the same metal oxidation levels (monochrome, thin tubes). Top: (**1**) Fe(II)–(μOH$^-$)*–Fe(II), showing alternative position of the monoxydroxo ligand, (**2**) Fe(II)–(μOH$^-$)–Fe(II)[*S*=4], total high-spin *S* = 4 (cyan), and (**3**) Fe(II)$^{[S=1]}$–(μOH$^-$)–Fe (II)$^{[S=1]}$, intermediate spin *S* = 1 for each Fe site (magenta). Bottom: (**1**) Fe(III)–(μOH$^-$)$_2$–Fe(III)[*S*=5], total high-spin *S* = 5 (cyan). For clarity, the protonations are shown only for the bridging μOH$^-$ ligands, which are depicted in ball-and-stick representation. The ball-and-stick representation applies as well to the two Fe sites and seven C_α (black) terminal carbon nuclei, the latter locked to their original X-ray crystal structure positions.

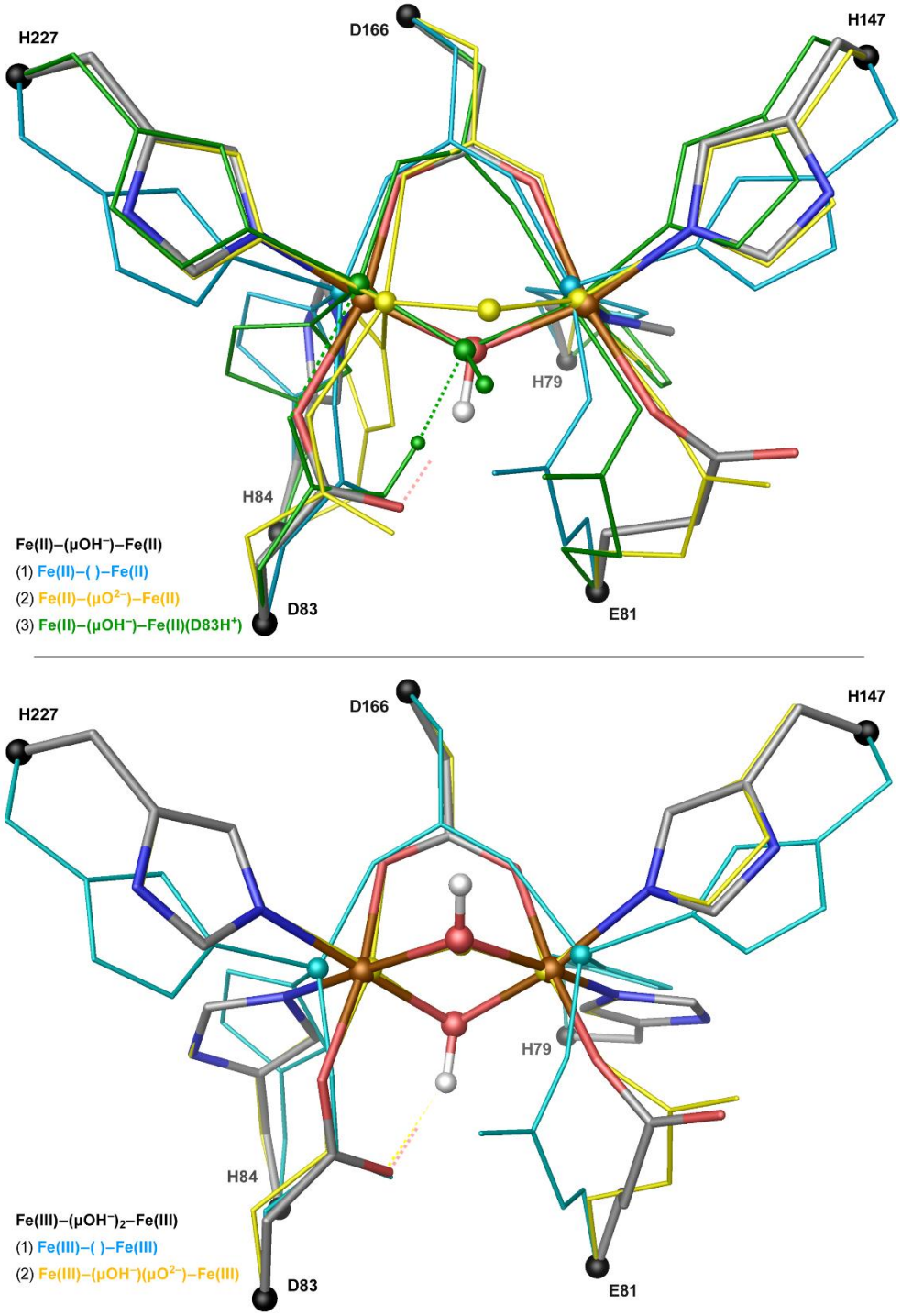

Fig. S13 Representative Fe(II)–(μOH$^-$)–Fe(II) (top) and Fe(III)–(μOH$^-$)$_2$–Fe(III) (bottom) DFT models of the FDP active site (element colors, tube representation), overlaid together with models showing either vacant bridging site or alternative protonation status (monochrome, thin tubes) as listed below. Top, Fe(II)Fe(II) oxidation level: (**1**) Fe(II)–( )–Fe(II) (cyan), (**2**) Fe(II)–(μO^{2-})–Fe(II) (yellow), and (**3**) Fe(II)–(μOH$^-$)–Fe(II)(D83H$^+$) (green). Bottom, Fe(III)Fe(III) oxidation level: (**1**) Fe(III)–( )–Fe(III) (cyan) and (**2**) Fe(III)–(μOH$^-$)(μO^{2-})–Fe(III) (yellow). For clarity, the protonations are shown only for the bridging oxygenous ligands and D83H$^+$ carboxylate, which are depicted in ball-and-stick representation. The ball-and-stick representation applies as well to the two Fe sites and seven C$_\alpha$ (black) terminal carbon nuclei, the latter locked to their original X-ray crystal structure positions.

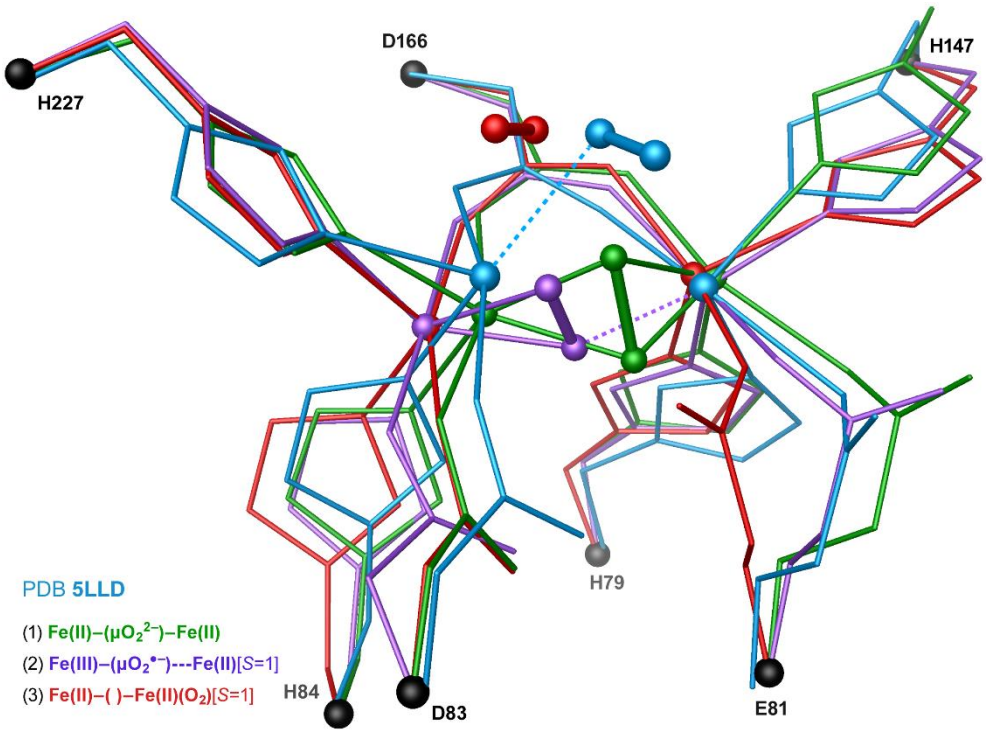

Fig. S14 DFT models of the FDP active site harboring alternative dioxygen species, overlaid with the reduced *E. coli* enzyme crystallographic structure (blue, PDB 5LLD[7]): (**1**) Fe(II)–(μO_2^{2-})–Fe(II) bridging peroxo (green), (**2**) Fe(III)–($\mu O_2^{\bullet-}$)···Fe(II)[*S*=1] semi-bridging superoxo, total spin *S* = 1 (purple), and (**3**) Fe(II)–( )–Fe(II)(O_2)[*S*=1] weakly bound molecular oxygen, total spin *S* = 1 (red). For clarity, the protein residue protonations are not shown. The dioxygen species are depicted in ball-and-stick representation. The ball-and-stick representation applies as well to the two Fe sites and seven C_α (black) terminal carbon nuclei, the latter locked to their original X-ray crystal structure positions.

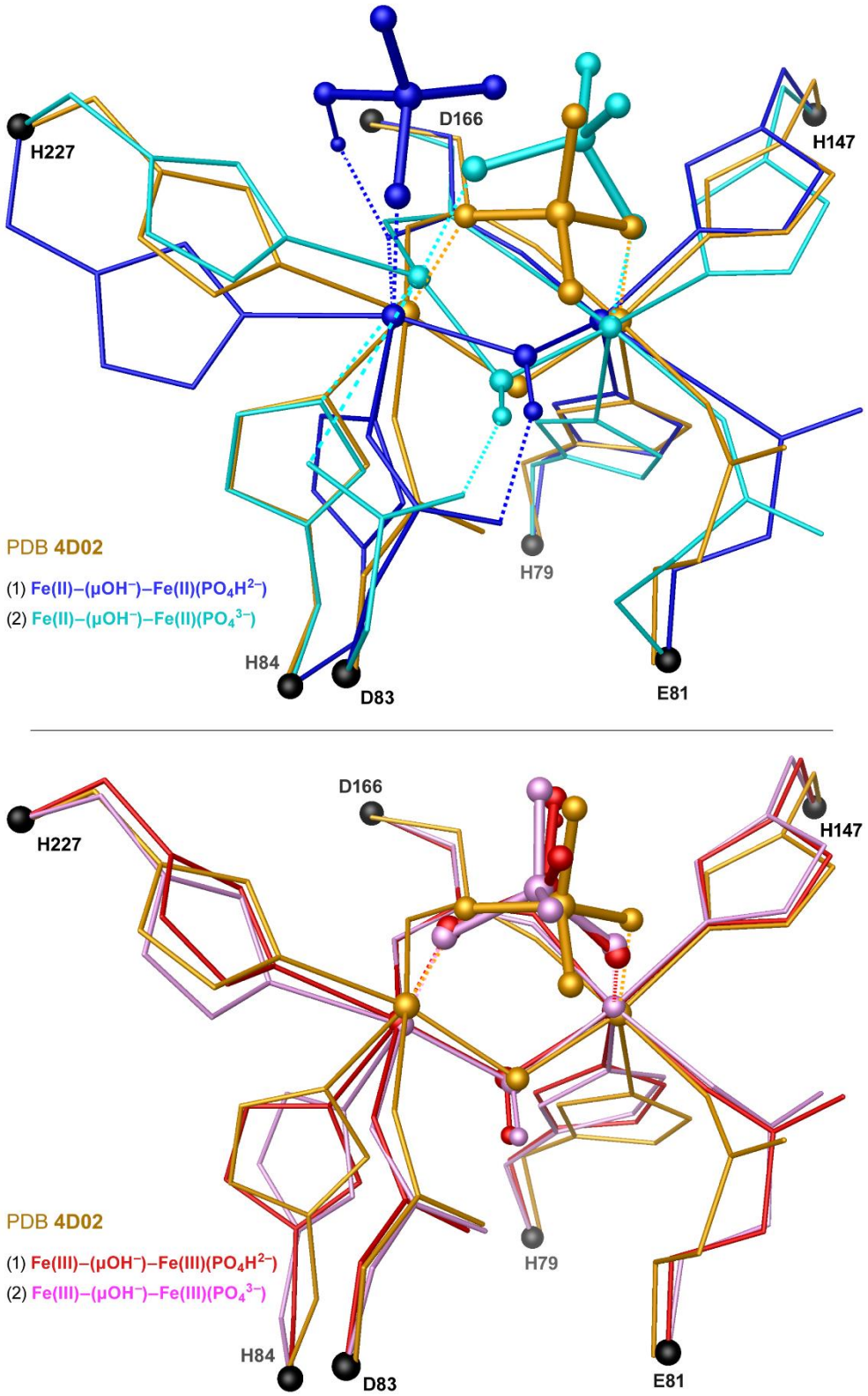

Fig. S15 DFT models of the FDP active site exploring alternatives of the phosphate anion coordination as found in the as-isolated *E. coli* enzyme crystallographic structure (beige, PDB 4D02[7]). Top, Fe(II)Fe(II) reduced level: (**1**) Fe(II)–(μOH$^-$)–Fe(II)(PO_4H^{2-}) (blue), (**2**) Fe(II)–(μOH$^-$)–Fe(II)(PO_4^{3-}) (cyan). Bottom, Fe(III)Fe(III) oxidised level: (**1**) Fe(III)–(μOH$^-$)–Fe(III)(PO_4H^{2-}) (red), (**2**) Fe(III)–(μOH$^-$)–Fe(III)(PO_4^{3-}) (pink). For clarity, the protonations are shown only for the bridging μOH$^-$ ligands and phosphate, which are depicted in ball-and-stick representation. The ball-and-stick representation applies as well to the two Fe sites and seven C_α (black) terminal carbon nuclei, the latter locked to their original X-ray crystal structure positions.

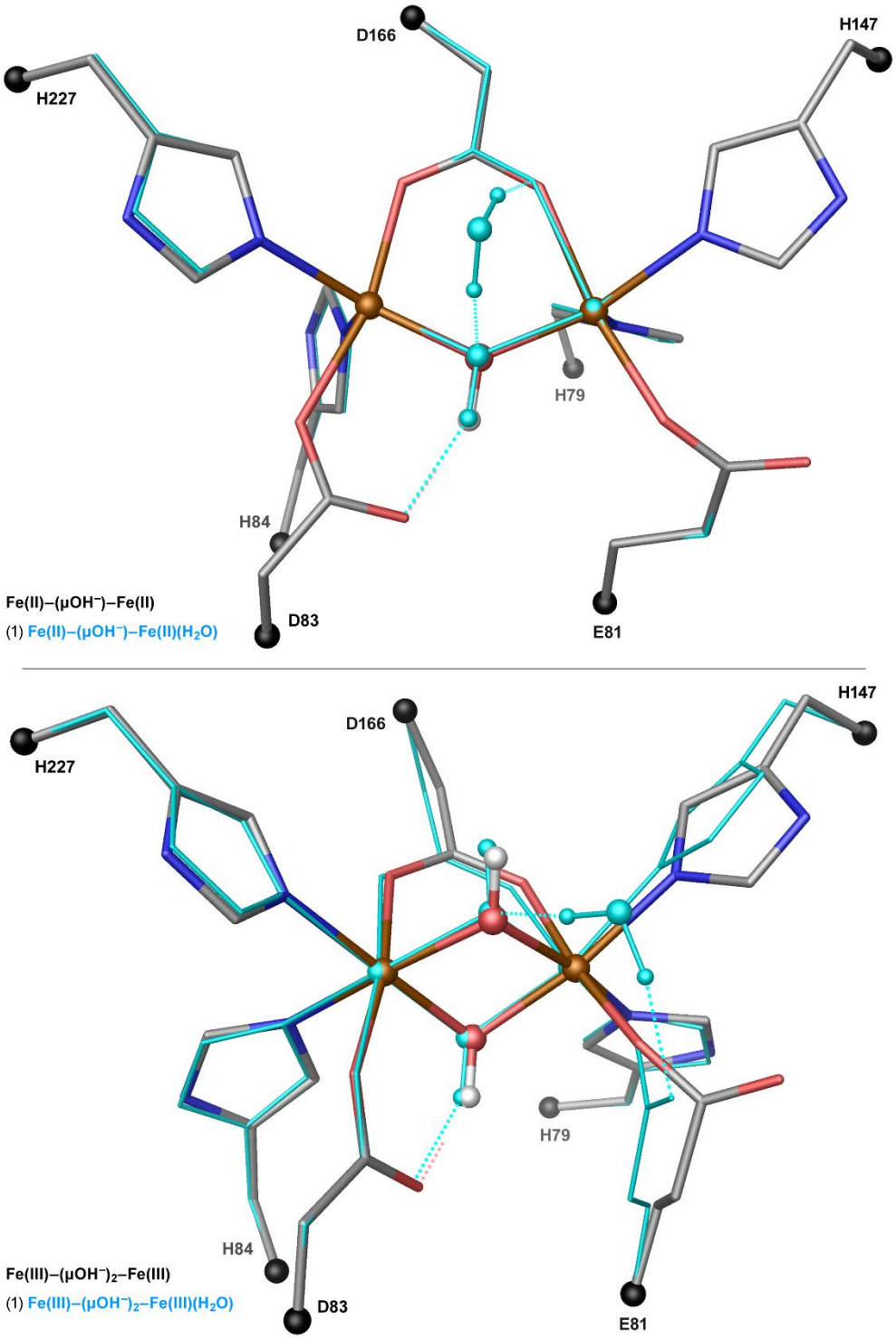

Fig. S16 Representative Fe(II)–(μOH⁻)–Fe(II) (top) and Fe(III)–(μOH⁻)$_2$–Fe(III) (bottom) DFT models of the FDP active site (element colors, tube representation), overlaid together with their alternatives including a solvent water molecule in hydrogen bonding contact to the bridging hydroxo ligand (cyan, thin tubes), top: (**1**) Fe(II)–(μOH⁻)–Fe(II)(H_2O), and bottom: (**1**) Fe(III)–(μOH⁻)$_2$–Fe(III)(H_2O). For clarity, the protonations are shown only for the bridging μOH⁻ ligands and H_2O molecule, which are depicted in ball-and-stick representation. The ball-and-stick representation applies as well to the two Fe sites and seven C_α (black) terminal carbon nuclei, the latter locked to their original X-ray crystal structure positions.

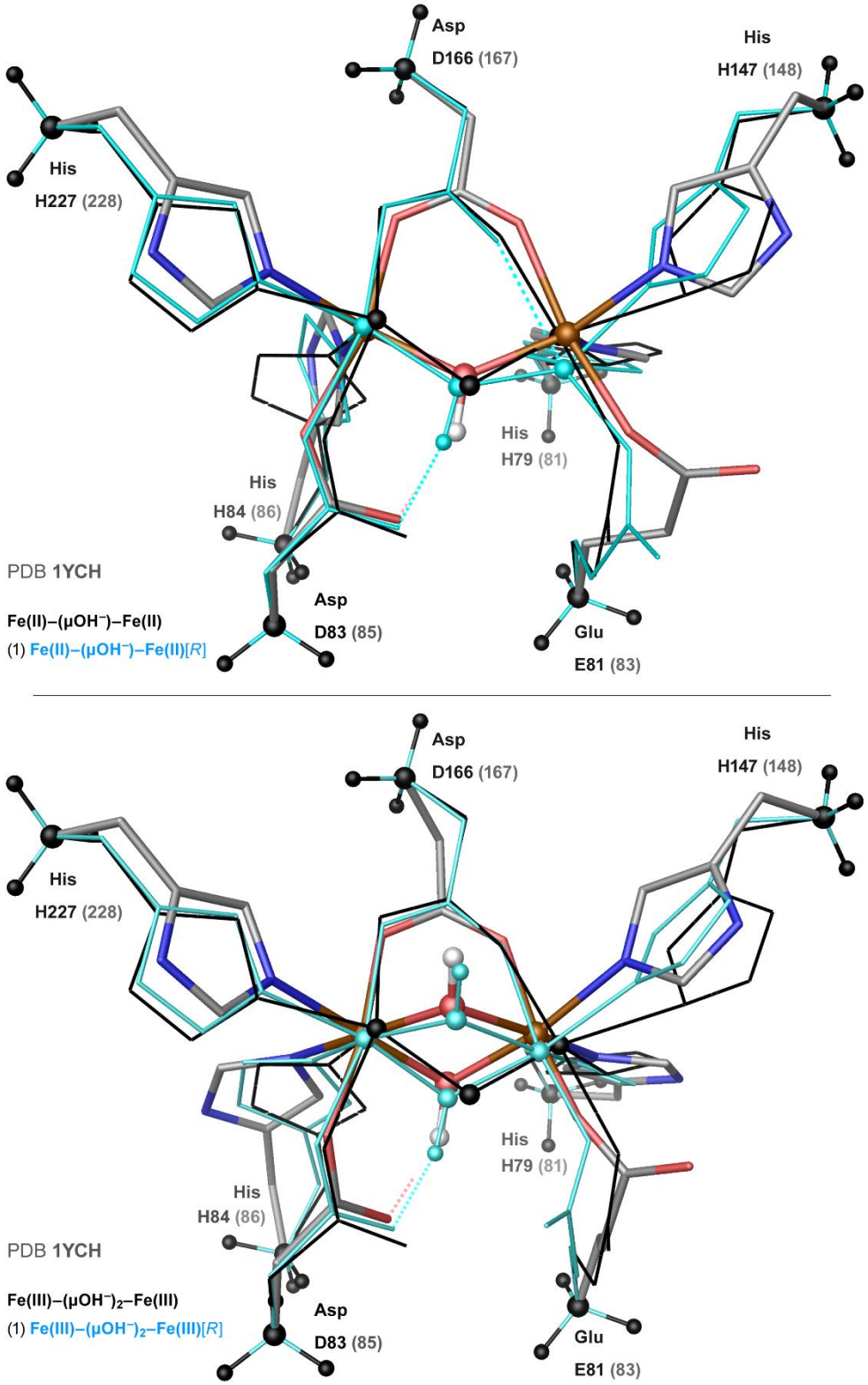

Fig. S17 Representative DFT-optimised models of the FDP active site in the reduced Fe(II)–(μOH⁻)–Fe(II) (top) and oxidised as-isolated Fe(III)–(μOH⁻)$_2$–Fe(III) (bottom) states (element colors, tube representation), overlaid with their alternatives exploring a rigid ("[*R*]") protein backbone framework with additional fixations of the entire –$C_\alpha H_3$ methyl terminal fragments (cyan, thin tubes), top: (**1**) Fe(II)–(μOH⁻)–Fe(II)[*R*], and bottom: (**1**) Fe(III)–(μOH⁻)$_2$–Fe(III)[*R*]. The overlay as well includes the X-ray crystal structure reference (*M. thermoacetica* FDP, PDB 1YCH,[6] black, wire representation). The bridging μOH⁻ ligands and the two Fe sites are depicted in ball-and-stick representation. This representation applies also to the fixed terminal fragments nuclei (black). The rest of the protons are omitted for clarity. The amino acid numbering shown corresponds to the sequences of FDP from *E. coli* (*M. thermoacetica*).

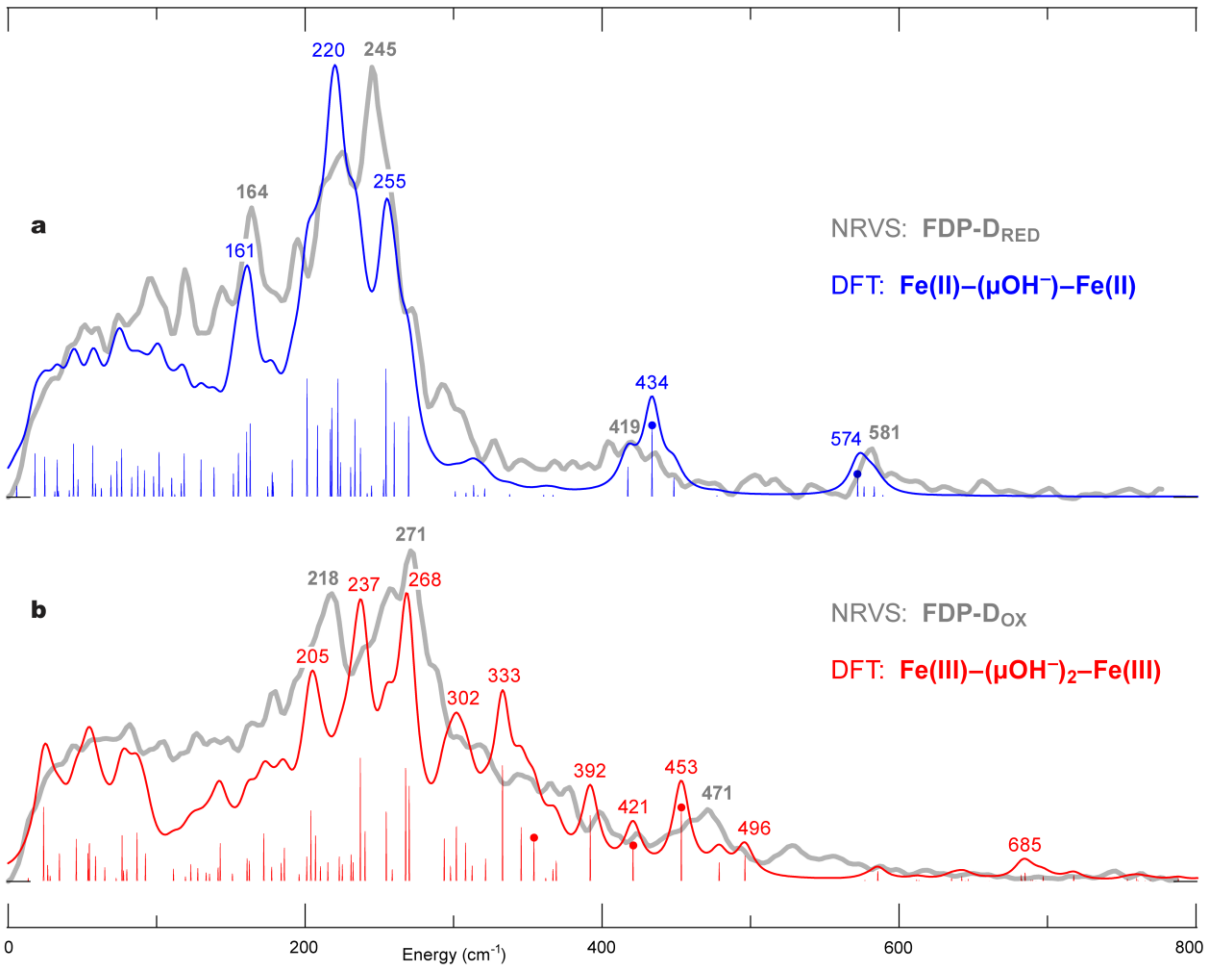

881

882 **Fig. S18** ^{57}Fe-PVDOS spectra of FDP-D in its (**a**) reduced and (**b**) oxidised states from NRVS experiments (grey
883 lines) and DFT calculations (blue/red lines) using the best-fit models shown in Figs. S9 or S10. Stick-style DFT data
884 is additionally provided, showing individual normal mode positions and their ^{57}Fe-PVDOS intensities. Selected
885 normal modes with significant Fe–μOH vibrational character are marked with dots and depicted in the main text
886 Fig. 4.

887

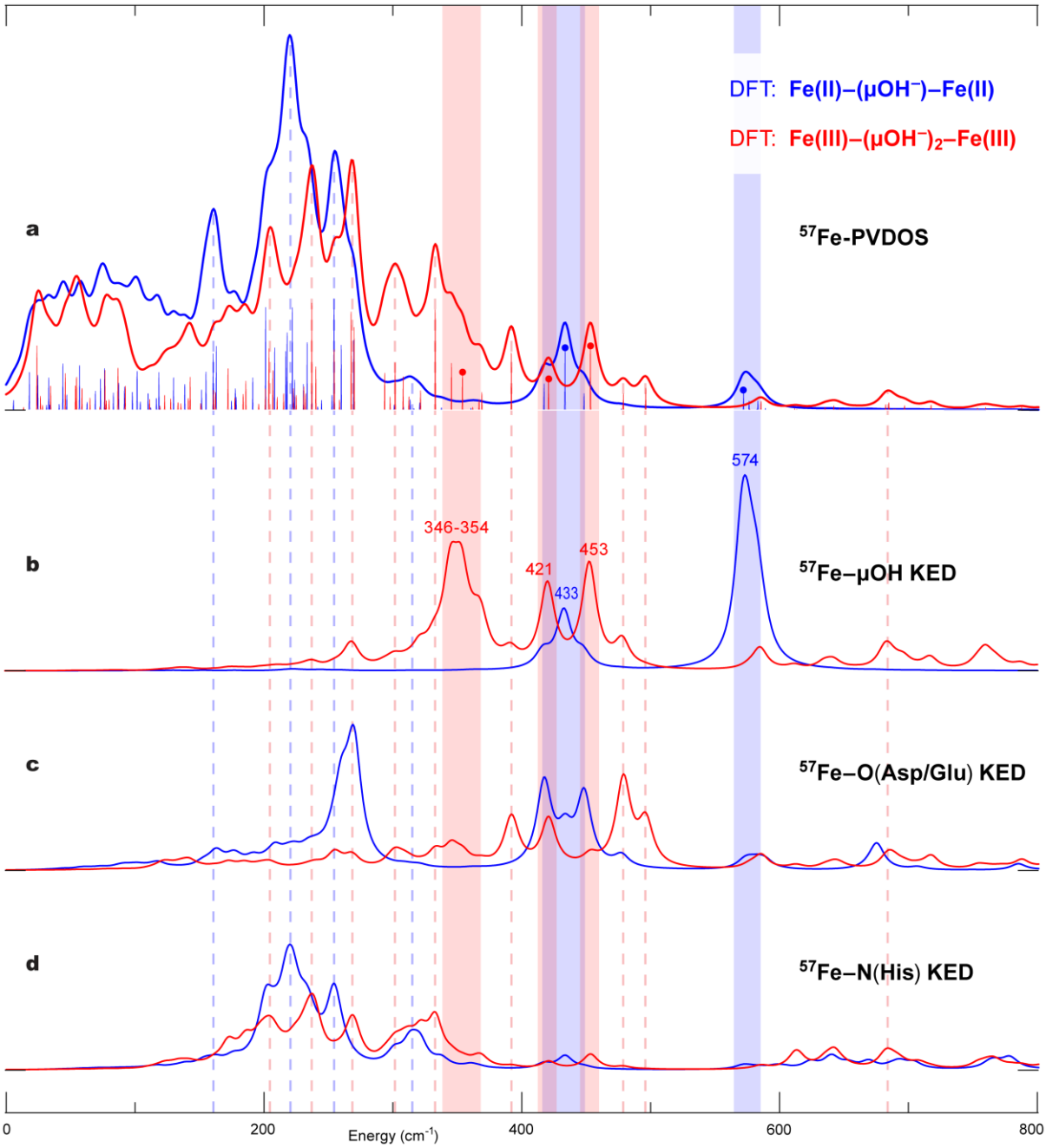

888

889 **Fig**. **S19** Vibrational analysis of the DFT-based (**a**) ^{57}Fe-PVDOS spectra in the FDP-D_{RED} reduced (blue, Fe(II)–(μOH$^-$
890)–Fe(II) model) and FDP-D_{OX} oxidised (red, Fe(III)–(μOH$^-$)$_2$–Fe(III) model) states using Fe–ligand interatomic
891 displacement KED profiles for the (**b**) ^{57}Fe–μO(H), (**c**) ^{57}Fe–O(Asp/Glu), and (**d**) ^{57}Fe–N(His) pairs. In (**a**), stick-style
892 DFT data is additionally provided, showing individual normal mode positions and their ^{57}Fe-PVDOS intensities.
893 Spectral regions with significant Fe–μOH vibrational character as deduced from (**b**) are highlighted using vertical
894 bars; selected normal modes of this character are marked with dots (and illustrated in the main text Fig. 4).

895

896

897

898

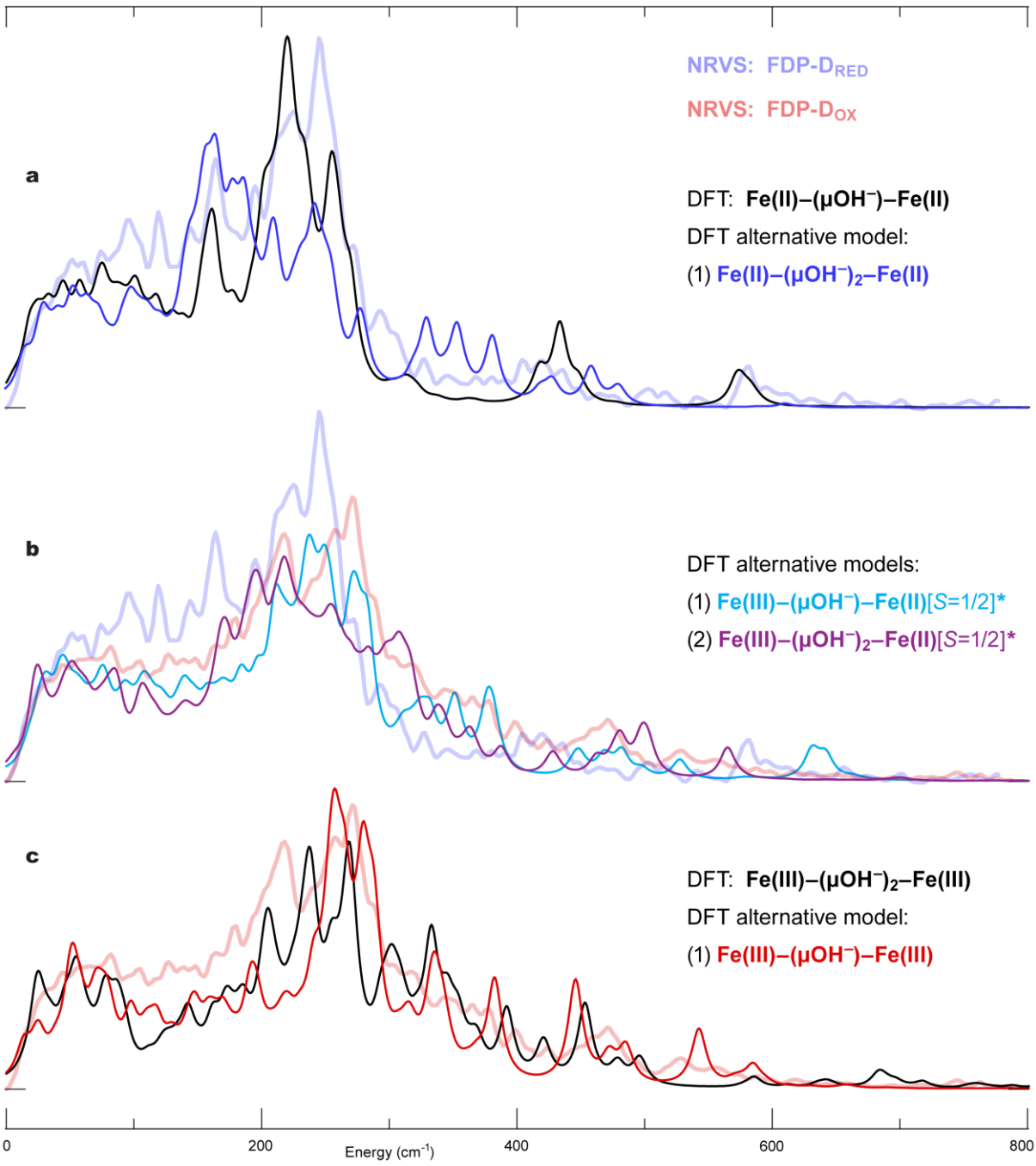

Fig. S20 ^{57}Fe-PVDOS spectra of FDP in its (**a**) Fe(II)Fe(II) reduced, (**b**) Fe(III)Fe(II) mixed-valence, and (**c**) Fe(III)Fe(III) oxidised states from DFT calculations using two isomer models at different oxidation levels as shown in Fig. S11. The DFT-predicted spectra are shown for both the representative (black lines) and alternative (lines in colour) models. For the mixed-valence systems in (**b**), the spectra are averaged (*) between the two Fe(III)Fe(II) and Fe(II)Fe(III) states (see text and Fig. S11). The ^{57}Fe-PVDOS spectra from the NRVS experiment (pale blue for FDP-D$_{RED}$ / red for FDP-D$_{OX}$) are overlaid with those from DFT for a comparison.

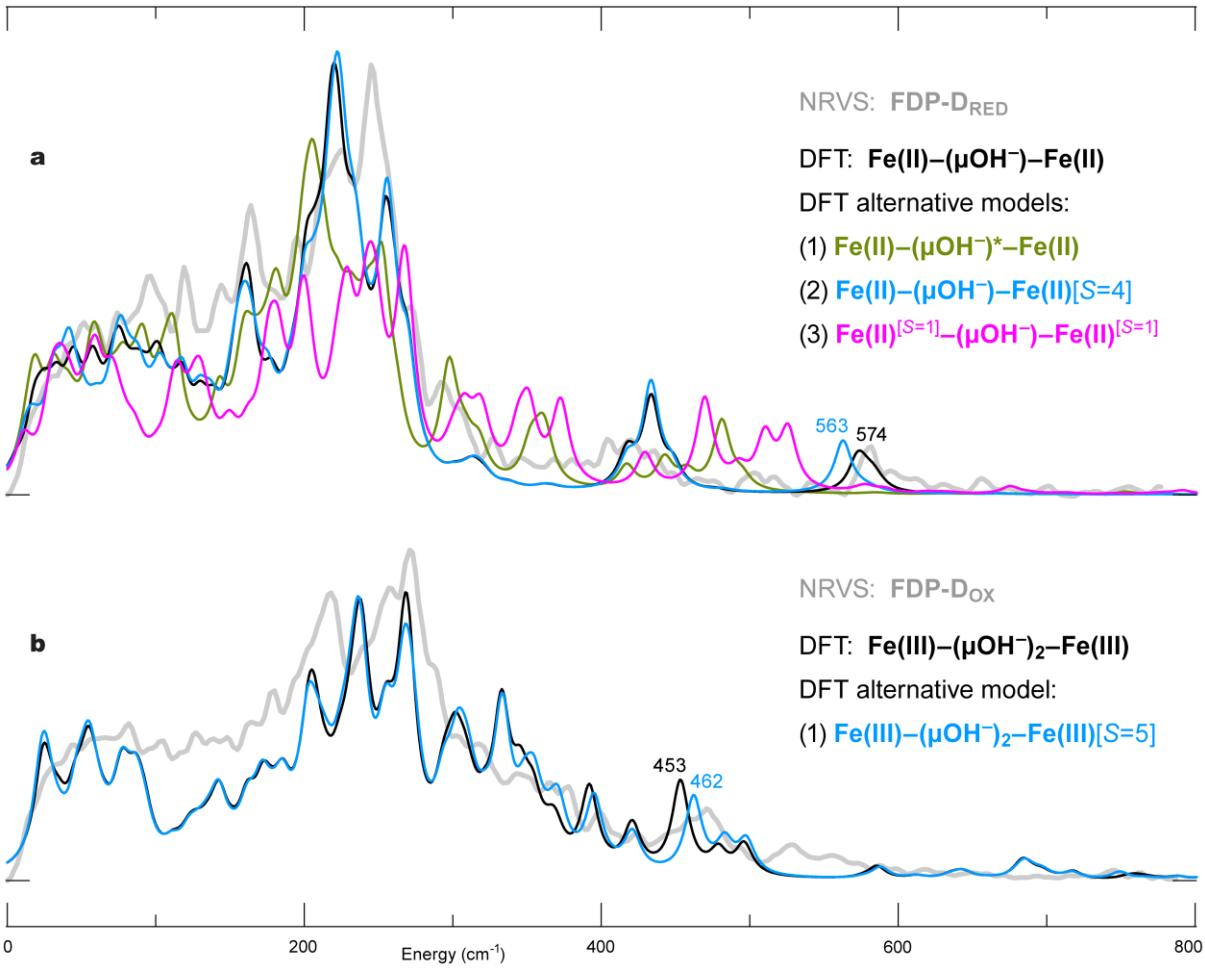

907

908 **Fig. S21** ^{57}Fe-PVDOS spectra of FDP-D in its (**a**) reduced and (**b**) oxidised states from NRVS experiment (grey lines)
909 and DFT calculations using representative models (black lines) and their isomers (lines in colour), shown in Fig.
910 S12. The models labelled with '*S*=…' numbers correspond to alternative electronic structures with either
911 individual Fe site ('$^{[S=...]}$') or total ('[*S*=…]') spin values different to the ground state.

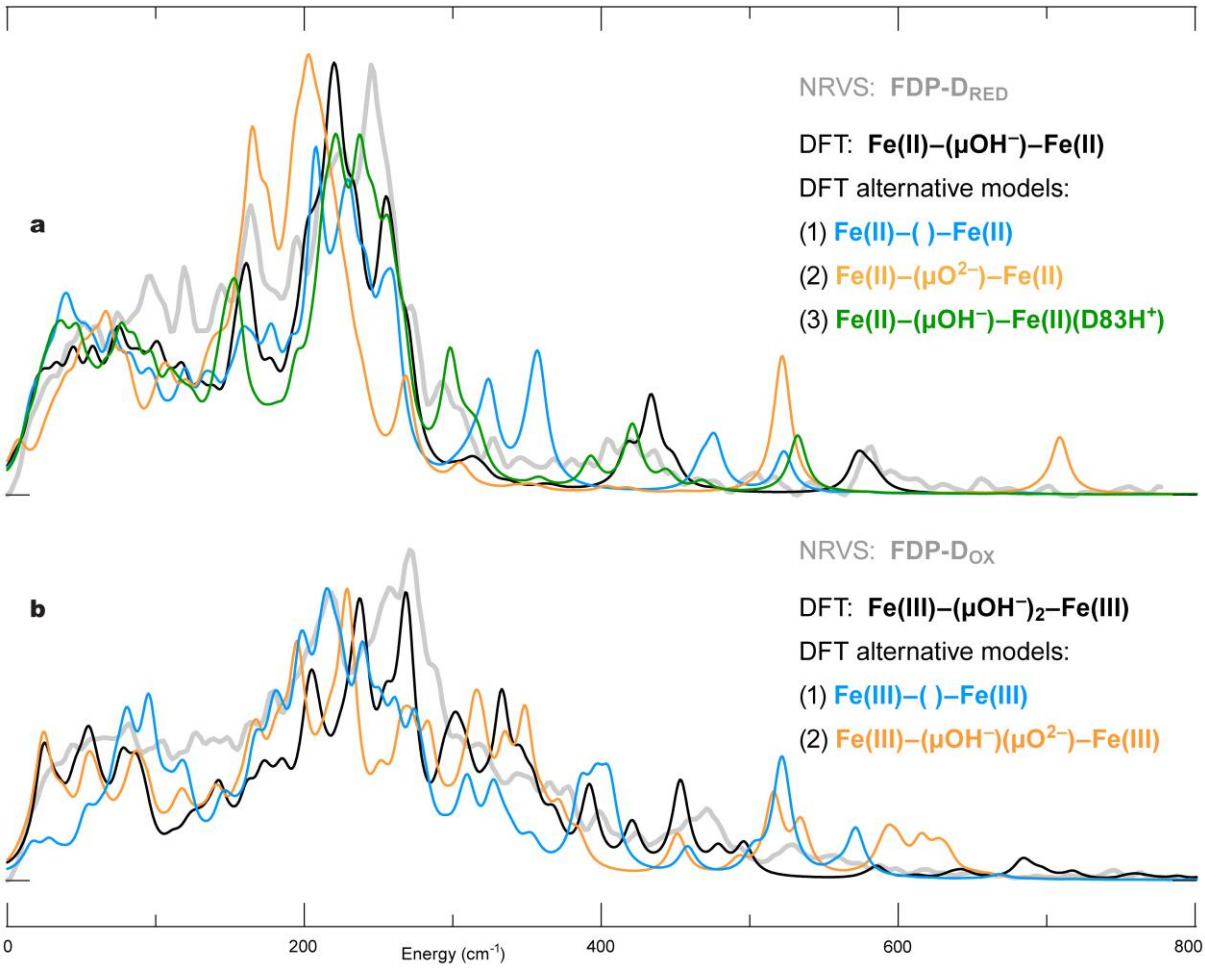

912

913 **Fig. S22** ^{57}Fe-PVDOS spectra of FDP-D in its (**a**) reduced and (**b**) oxidised states from NRVS experiment (grey lines)
914 and DFT calculations using models shown in Fig. S13. The DFT-predicted spectra are shown for both the
915 representative (black lines) and alternative (lines in colour) models.

916

917

918

919

920

921

922

923

924

925

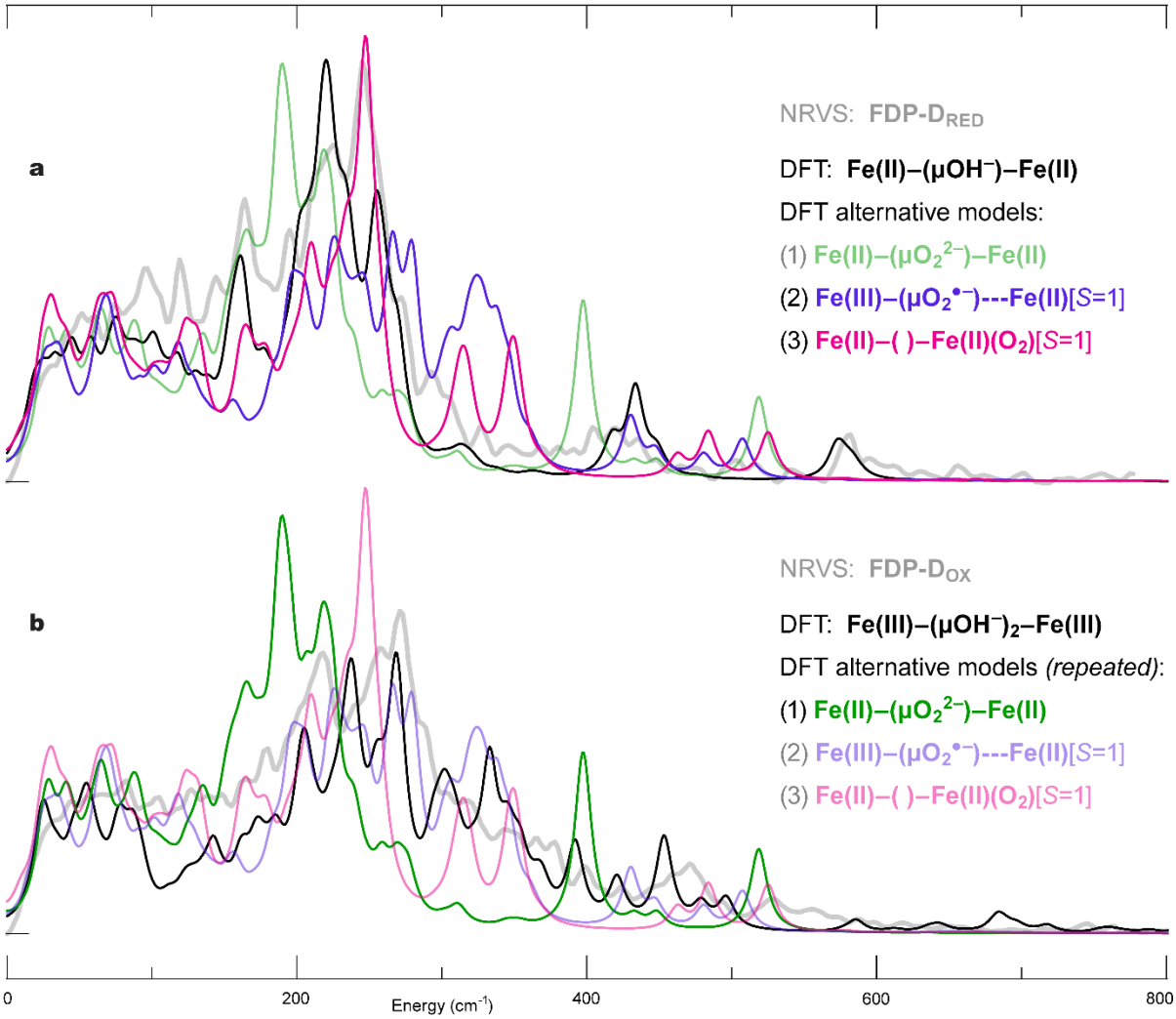

Fig. S23 ^{57}Fe-PVDOS spectra of FDP-D in its (**a**) reduced and (**b**) oxidised states from NRVS experiment (grey lines) and DFT calculations using representative models (black lines), and models that produced alternative dioxygen species (lines in colour) as shown in Fig. S14. The dioxygen species spectra repeat twice in (**a**) and (**b**), with lines in pale for those models that initially implied a different Fe-s oxidation level as explained in Supplementary Results and Discussion, subsection (*v*).

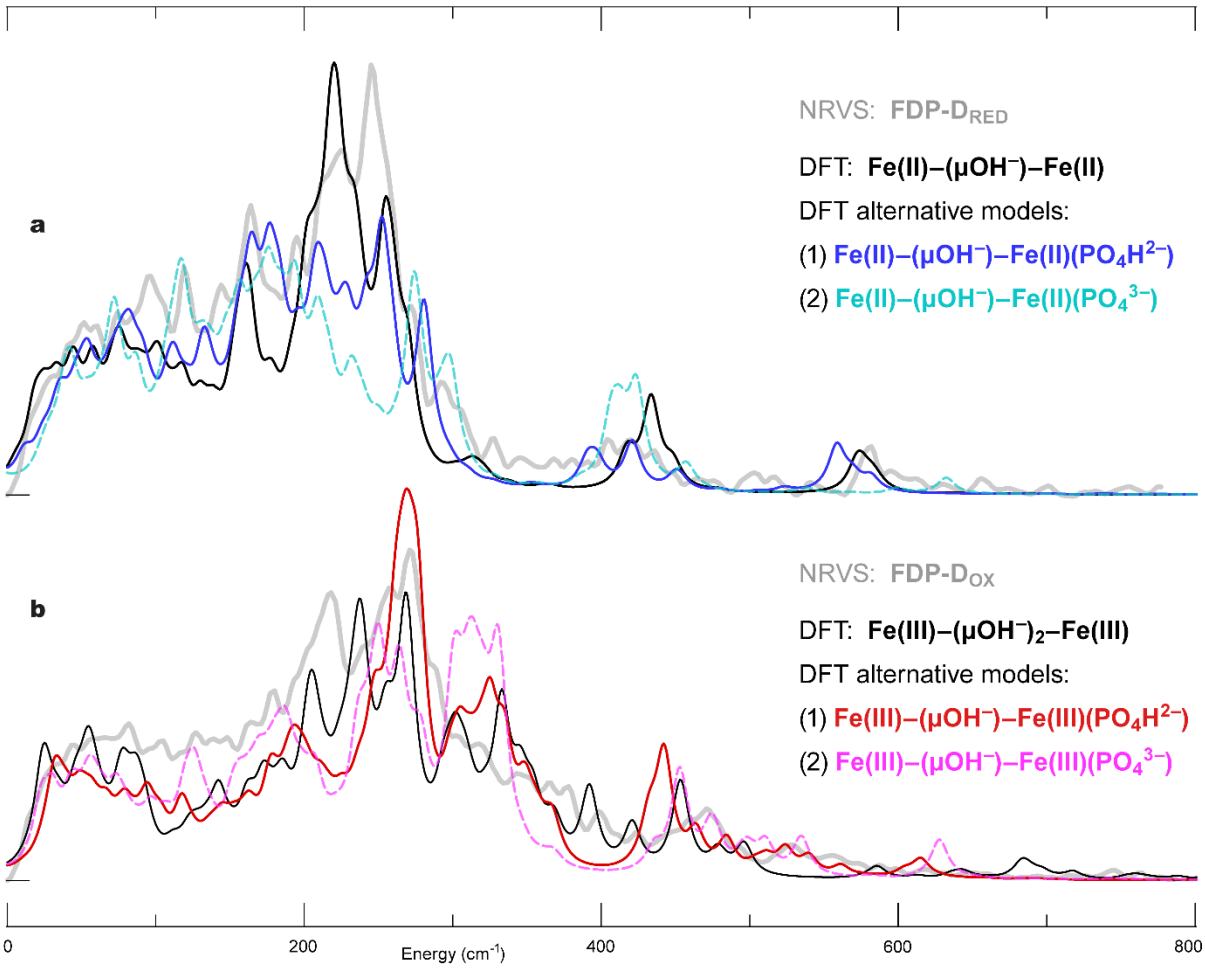

Fig. S24 ^{57}Fe-PVDOS spectra of FDP-D in its (**a**) reduced and (**b**) oxidised states from NRVS experiment (grey lines) and DFT calculations using models including the phosphate anion (lines in colour) as shown in Fig. S15. The DFT-predicted spectra are additionally shown for the representative models (black lines).

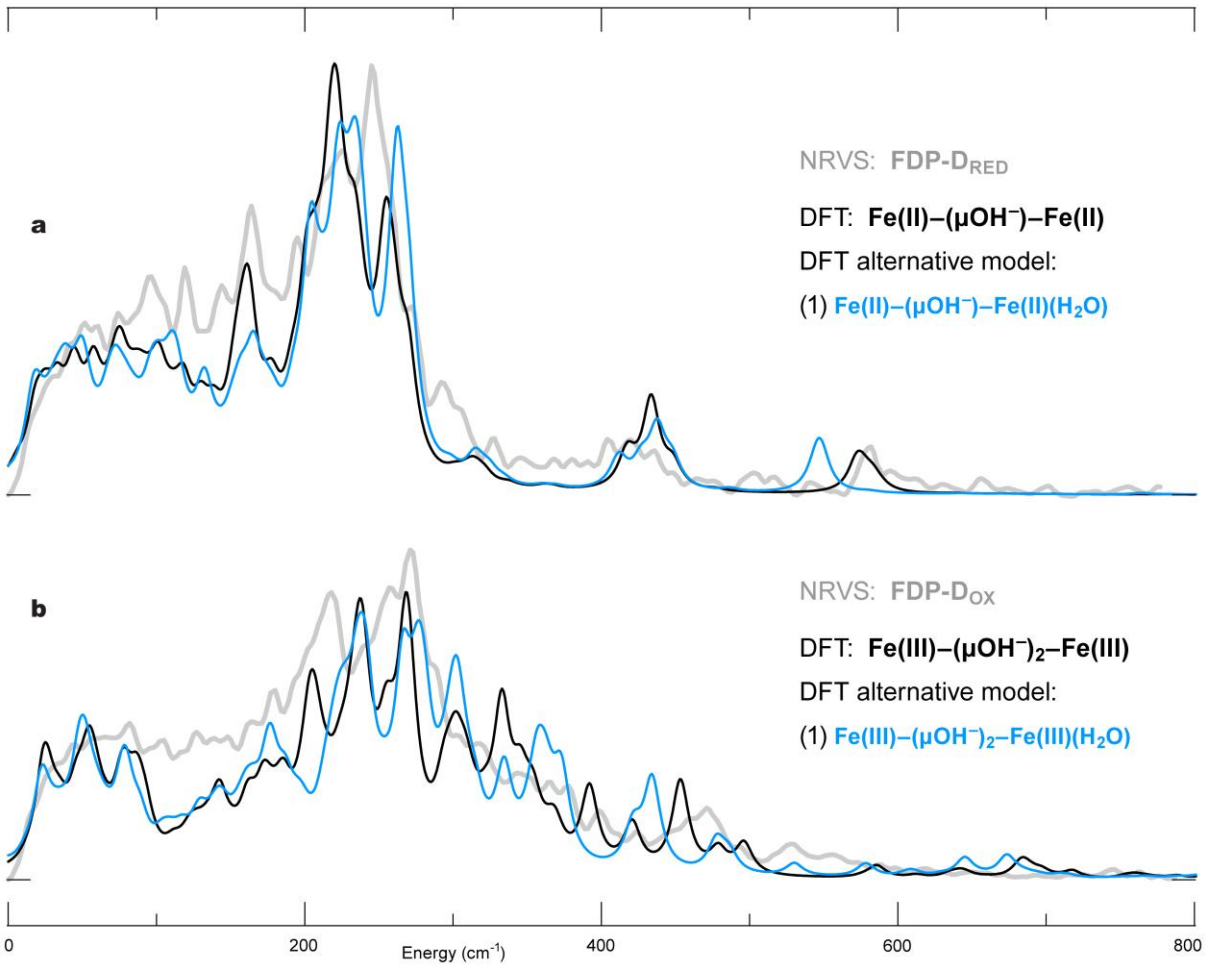

958

959 **Fig. S25** ^{57}Fe-PVDOS spectra of FDP-D in its (**a**) reduced and (**b**) oxidised states from NRVS experiment (grey lines)
960 and DFT calculations using models including a solvent water molecule inclusion (lines in cyan) as shown in Fig.
961 S16. The DFT-predicted spectra are additionally shown for the representative models (black lines).

962

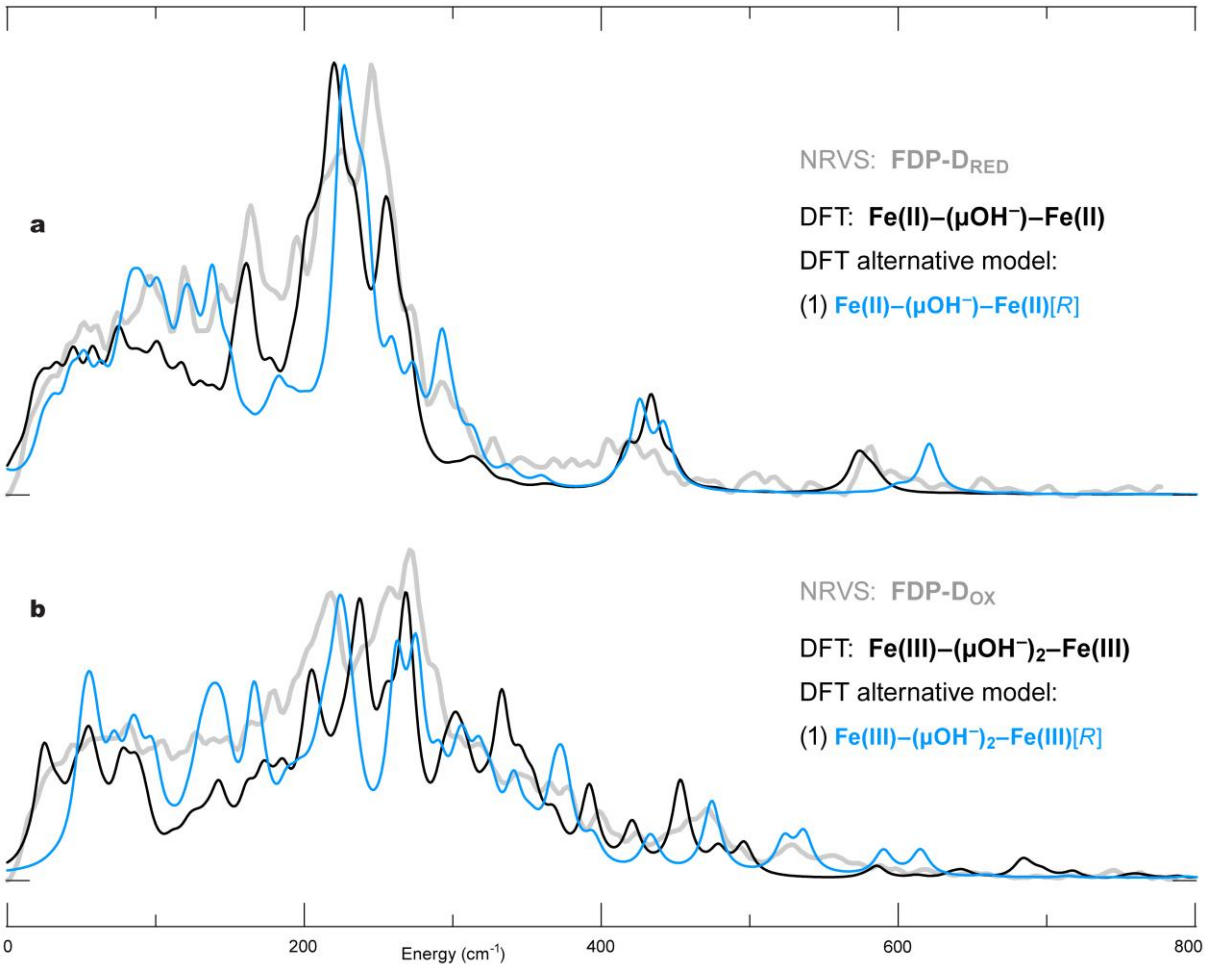

963

964 **Fig. S26** ^{57}Fe-PVDOS spectra of FDP-D in its (**a**) reduced and (**b**) oxidised states from NRVS experiment (grey lines)
965 and DFT calculations using models exploring a rigid ("[*R*]") protein backbone framework with additional fixations
966 of the entire $-C_\alpha H_3$ methyl terminal fragments (lines in cyan) as shown in Fig. S17. The DFT-predicted spectra are
967 additionally shown for the representative models (black lines).

968

969

970

971

972

973

974

975

976

977

978

979

References

1. J. B. Vicente and M. Teixeira, *J. Biol. Chem.*, 2005, **280**, 34599-34608.
2. F. Folgosa, M. C. Martins and M. Teixeira, *Sci. Rep.*, 2018, **8**, 10164.
3. L. Lauterbach, H. X. Wang, M. Horch, L. B. Gee, Y. Yoda, Y. Tanaka, I. Zebger, O. Lenz and S. P. Cramer, *Chem. Sci.*, 2015, **6**, 1055-1060.
4. L. B. Gee, H. X. Wang and S. P. Cramer, *Methods Enzymol.*, 2018, **599**, 409-425.
5. W. Sturhahn, *Hyperfine Interact.*, 2000, **125**, 149-172.
6. R. Silaghi-Dumitrescu, D. M. Kurtz, Jr., L. G. Ljungdahl and W. N. Lanzilotta, *Biochemistry*, 2005, **44**, 6492-6501.
7. C. V. Romao, J. B. Vicente, P. T. Borges, B. L. Victor, P. Lamosa, E. Silva, L. Pereira, T. M. Bandeiras, C. M. Soares, M. A. Carrondo, D. Turner, M. Teixeira and C. Frazao, *J. Mol. Biol.*, 2016, **428**, 4686-4707.
8. M. J. Frisch, G. W. Trucks, H. B. Schlegel, G. E. Scuseria, M. A. Robb, J. R. Cheeseman, G. Scalmani, V. Barone, B. Mennucci, G. A. Petersson, H. Nakatsuji, M. Caricato, X. Li, H. P. Hratchian, A. F. Izmaylov, J. Bloino, G. Zheng, J. L. Sonnenberg, M. Hada, M. Ehara, K. Toyota, R. Fukuda, J. Hasegawa, M. Ishida, T. Nakajima, Y. Honda, O. Kitao, H. Nakai, T. Vreven, J. A. Montgomery, Jr., J. E. Peralta, F. Ogliaro, M. Bearpark, J. J. Heyd, E. Brothers, K. N. Kudin, V. N. Staroverov, R. Kobayashi, J. Normand, K. Raghavachari, A. Rendell, J. C. Burant, S. S. Iyengar, J. Tomasi, M. Cossi, N. Rega, J. M. Millam, M. Klene, J. E. Knox, J. B. Cross, V. Bakken, C. Adamo, J. Jaramillo, R. Gomperts, R. E. Stratmann, O. Yazyev, A. J. Austin, R. Cammi, C. Pomelli, J. W. Ochterski, R. L. Martin, K. Morokuma, V. G. Zakrzewski, G. A. Voth, P. Salvador, J. J. Dannenberg, S. Dapprich, A. D. Daniels, Ö. Farkas, J. B. Foresman, J. V. Ortiz, J. Cioslowski and D. J. Fox, *Gaussian 09, Revision D.01, Gaussian Inc., Wallingford CT, 2009*.
9. *Jaguar, version 9.4, Schrodinger, Inc., New York, NY, 2016.*
10. L. Noodleman and D. A. Case, *Adv. Inorg. Chem.*, 1992, **38**, 423-470.
11. C. Adamo and V. Barone, *J. Chem. Phys.*, 1999, **110**, 6158-6170.
12. J. Tomasi, B. Mennucci and R. Cammi, *Chem. Rev.*, 2005, **105**, 2999-3093.
13. S. Grimme, J. Antony, S. Ehrlich and H. Krieg, *J. Chem. Phys.*, 2010, **132**, 154104.
14. L. Goerigk and S. Grimme, *Phys. Chem. Chem. Phys.*, 2011, **13**, 6670-6688.
15. D. Mitra, V. Pelmenschikov, Y. Guo, D. A. Case, H. Wang, W. Dong, M. L. Tan, T. Ichiye, F. E. Jenney, M. W. Adams, Y. Yoda, J. Zhao and S. P. Cramer, *Biochemistry*, 2011, **50**, 5220-5235.
16. A. C. Weitz, N. Giri, J. D. Caranto, D. M. Kurtz, Jr., E. L. Bominaar and M. P. Hendrich, *J. Am. Chem. Soc.*, 2017, **139**, 12009-12019.
17. A. C. Weitz, E. A. Hill, V. F. Oswald, E. L. Bominaar, A. S. Borovik, M. P. Hendrich and Y. S. Guo, *Angew. Chem. Int. Ed.*, 2018, **57**, 16010-16014.
18. K. Park and E. I. Solomon, *Can. J. Chem.*, 2014, **92**, 975-978.
19. D. M. Kurtz, D. F. Shriver and I. M. Klotz, *Coord. Chem. Rev.*, 1977, **24**, 145-178.
20. M. Wirstam, S. J. Lippard and R. A. Friesner, *J. Am. Chem. Soc.*, 2003, **125**, 3980-3987.
21. M. A. Holmes, I. Letrong, S. Turley, L. C. Sieker and R. E. Stenkamp, *J. Mol. Biol.*, 1991, **218**, 583-593.
22. T. C. Brunold and E. I. Solomon, *J. Am. Chem. Soc.*, 1999, **121**, 8288-8295.
23. B. G. Fox, M. P. Hendrich, K. K. Surerus, K. K. Andersson, W. A. Froland, J. D. Lipscomb and E. Munck, *J. Am. Chem. Soc.*, 1993, **115**, 3688-3701.
24. A. C. Rosenzweig, P. Nordlund, P. M. Takahara, C. A. Frederick and S. J. Lippard, *Chem. Biol.*, 1995, **2**, 409-418.
25. J. B. Lynch, C. Juarez-Garcia, E. Munck and L. Que, Jr., *J. Biol. Chem.*, 1989, **264**, 8091-8096.
26. P. Nordlund, B. M. Sjoberg and H. Eklund, *Nature*, 1990, **345**, 593-598.
27. M. H. Sazinsky, J. Bard, A. Di Donato and S. J. Lippard, *J. Biol. Chem.*, 2004, **279**, 30600-30610.
28. J. D. Pikus, J. M. Studts, C. Achim, K. E. Kauffmann, E. Munck, R. J. Steffan, K. McClay and B. G. Fox, *Biochemistry*, 1996, **35**, 9106-9119.
29. W. G. Han, T. Liu, T. Lovell and L. Noodleman, *J. Comput. Chem.*, 2006, **27**, 1292-1306.
30. J. C. Jones, R. Banerjee, K. Shi, H. Aihara and J. D. Lipscomb, *Biochemistry*, 2020, **59**, 2946-2961.
31. D. T. Logan, X. D. Su, A. Aberg, K. Regnstrom, J. Hajdu, H. Eklund and P. Nordlund, *Structure*, 1996, **4**, 1053-1064.